NASA CONTRACTOR REPORT

NASA CR-2759

NASA CR-2759

PRELIMINARY STUDY OF CONTAMINANT PARTICULATES AROUND SKYLAB

D. W. Schuerman and J. L. Weinberg

Prepared by
STATE UNIVERSITY OF NEW YORK AT ALBANY
Albany, N.Y. 12203
for George C. Marshall Space Flight Center

NATIONAL AERONAUTICS AND SPACE ADMINISTRATION • WASHINGTON, D. C. • OCTOBER 1976

1. Report No.	2. Government Accession No.	3. Recipient's Catalog No.
NASA CR-2759		

4. Title and Subtitle	5. Report Date
Preliminary Study of Contaminant Particulates around Skylab	October 1976
	6. Performing Organization Code

7. Author(s)	8. Performing Organization Report No.
D. W. Schuerman and L. L. Weinberg	M-187
	10. Work Unit No.

9. Performing Organization Name and Address	11. Contract or Grant No.
Space Astronomy Laboratory State University of New York at Albany Albany, New York 12203	NAS8-31902
	13. Type of Report and Period Covered
12. Sponsoring Agency Name and Address	Contractor
National Aeronautics and Space Administration Washington, D. C. 20546	14. Sponsoring Agency Code

15. Supplementary Notes

16. Abstract

Techniques originally developed for the Skylab T025 contamination experiment were applied to S052 white-light coronagraph data in a preliminary study to investigate particulates around Skylab. Periods were selected which contained some contamination, even though there were no apparent dumps or vents during these periods. For the first time, velocity and size distributions were determined from optical data for particles within 200 meters of the spacecraft. Both photographic (61 particle tracks) and video (34 particles) observations yield an upper limit on particle radius of 100 μm. The smallest particle observed had a radius of 5 μm, but this limit is imposed by the sensitivity of the coronagraph and does not reflect a true lower cutoff of the size distribution. The typical particle velocity as determined from the video data was 1 m/s. The number density of particulates within 200 meters of the spacecraft was found to vary from approximately 10^{-9}/cm^3 to 2×10^{-8}/cm^3 (from 5 to 100 particles per field of view).

Selected photometric data from the S073 zodiacal light experiment during mission SL-2 were also examined for evidence of contamination. Contrary to the results of an analysis of these same data by Muscari and Jambor (Skylab experiment T027), we find no evidence for a detectable spacecraft corona. Although the photometer data were taken at different times, this result is consistent with the S052 analysis which finds the typical number density of particles larger than 5 μm to be at or below the photometer's 1 to 3 $S_{10}(V)$ column brightness threshold for detection.[1] Since particles smaller than 5 μm are expected to be present, the brightness of the spacecraft corona should be even brighter than that predicted by the S052 data.

This study demonstrates the need for further joint observations and correlative studies of single particle data as obtained from an imaging system and particle cloud data obtained from a photometer system: this would make possible an accurate prediction of the effect on one from the results of the other and a more complete description of the contaminant cloud.

[1]Equivalent number of 10th magnitude solar (G2V) stars per square degree at mean solar distance. At 5300 Å, $1\ S_{10}(V) = 4.5 \times 10^{-16}\ B_{\odot}$.

17. Key Words (Suggested by Author(s))	18. Distribution Statement
Contamination Scattered light Small particles Coronagraph	Category 88

19. Security Classif. (of this report)	20. Security Classif. (of this page)	21. No. of Pages	22. Price*
Unclassified	Unclassified	86	$4.75

For sale by the National Technical Information Service, Springfield, Virginia 22161

AUTHORS' ACKNOWLEDGMENTS

We wish to thank Dr. R. M. MacQueen, Principal Investigator of the Skylab S052 coronagraph experiment, for his help, his interest, and his data. The initial planning of this investigation was done in collaboration with Frank Giovane, Co-Investigator of the Skylab T025 experiment, who, in anticipation of this analysis, had digitized the photographic data soon after the mission. We thank Richard Hahn for devising quantitative methods for extracting results from the video data. This study was supported by NASA contract NAS8-31902.

TABLE OF CONTENTS

I. Analysis of Photographic and Video Tape Data, Experiment S052

Introduction

The S052 white light coronagraph on Skylab produced over 35,000 photographs of the solar corona. Approximately 10% of these frames contain evidence of particulates in the environs of the spacecraft. The monitoring of this contamination was one of the prime objectives of another coronagraph experiment, T025, (Henize and Weinberg, 1973) but because the solar-side airlock was rendered useless throughout the mission, that T025 objective could not be performed. Therefore, the S052 "contaminated" frames constitute a unique body of data which represents most, if not all, of the existing observations of spacecraft-induced particulates. Since particulates of this sort can be the limiting factor for optical and infrared experiments, it is important to ascertain what information can be inferred about them from the S052 photographs. As a preliminary to a larger, statistical study, this investigation attempts (1) to define the S052 limits of particle detectability, (2) to enumerate which particulate parameters can be inferred, and (3) to note the accuracy with which these parameters can be found in practice. The techniques used here are those developed by us for the anticipated reduction of T025 data.

The actual film used in this pilot study is a first generation copy of eleven sequential S052 frames containing particle tracks. This film, along with pertinent instrumental data, has been provided by R. MacQueen, the Principal Investigator of the S052 Experiment. This photographic sequence, initiated on day of year (DOY) 159 at 0200 GMT, was selected only on the basis that it is representative of the contamination data.

Theory

A nearby particle moving within the field of view of the S052 white light coronagraph registers as a track of width, a, and length, l, on the film. The width of the track is defined by the circle-of-confusion (here assumed uniform) resulting from an out-of-focus point source and is a measure of the particle's distance, L, from the instrument. Since the coronagraph is focused at infinity, a and L are related by

$$a = \frac{Af}{L} \qquad \text{for } a \gtrsim e \tag{1}$$

where A is the diameter of the objective, f is the focal length, and e is the resolution of the system. When L is less than about 200 meters, a is larger than e and the particle's distance can be obtained directly from the film. The two other space coordinates of the particle (X,Y) can be found from the particle's film coordinates (x,y):

$$\frac{X}{L} = \frac{x}{f} \qquad \text{and} \qquad \frac{Y}{L} = \frac{y}{f} \; . \tag{2}$$

The space velocity of the particle can only be obtained (except for sign) if the track under consideration is entirely contained within a single photograph. Consider any two points on the track separated by a distance on the film of Δl. It can be shown that the time required for the particle image to traverse Δl is related to the frame exposure time, T, by

$$t = \frac{\Delta l}{l} T \qquad \text{provided } \frac{\Delta l}{f} \ll \sqrt{\left(\frac{\Delta X}{\Delta L}\right)^2 + \left(\frac{\Delta Y}{\Delta L}\right)^2} \; . \tag{3}$$

The inequality always holds except for those few particles whose motion is mostly along the line of sight. Therefore, the transverse and radial space velocities are found by

$$V_r = \frac{\Delta L}{\Delta t} \quad \text{and} \quad V_t = \sqrt{\frac{(\Delta X)^2 + (\Delta Y)^2}{(\Delta t)^2}} \; . \tag{4}$$

The transverse space velocity, in turn, is related to the rate of image motion across the film by

$$v = \frac{f\, V_t}{L} \; . \tag{5}$$

It is this image motion which determines an effective particle exposure time, τ. At the center of the track, an elemental area of the film is exposed to the moving circle-of-confusion of diameter a for a time

$$\tau = \frac{a}{v} = \frac{a\, L}{f\, V_t} = \frac{A}{V_t} \; . \tag{6}$$

The film density of the particle track thus depends on τ, while the film background depends on the frame exposure time T.

Further photometric considerations of the particle track can be used to infer the actual size of the particle. The energy/area incident on the film in the center of a track can be calculated if the spectral sensitivity of the system is known. The wavelength response of the S052 coronagraph is shown in Figure 1. The monochromatic energy response of the film due to an out-of-focus particle image is then given by

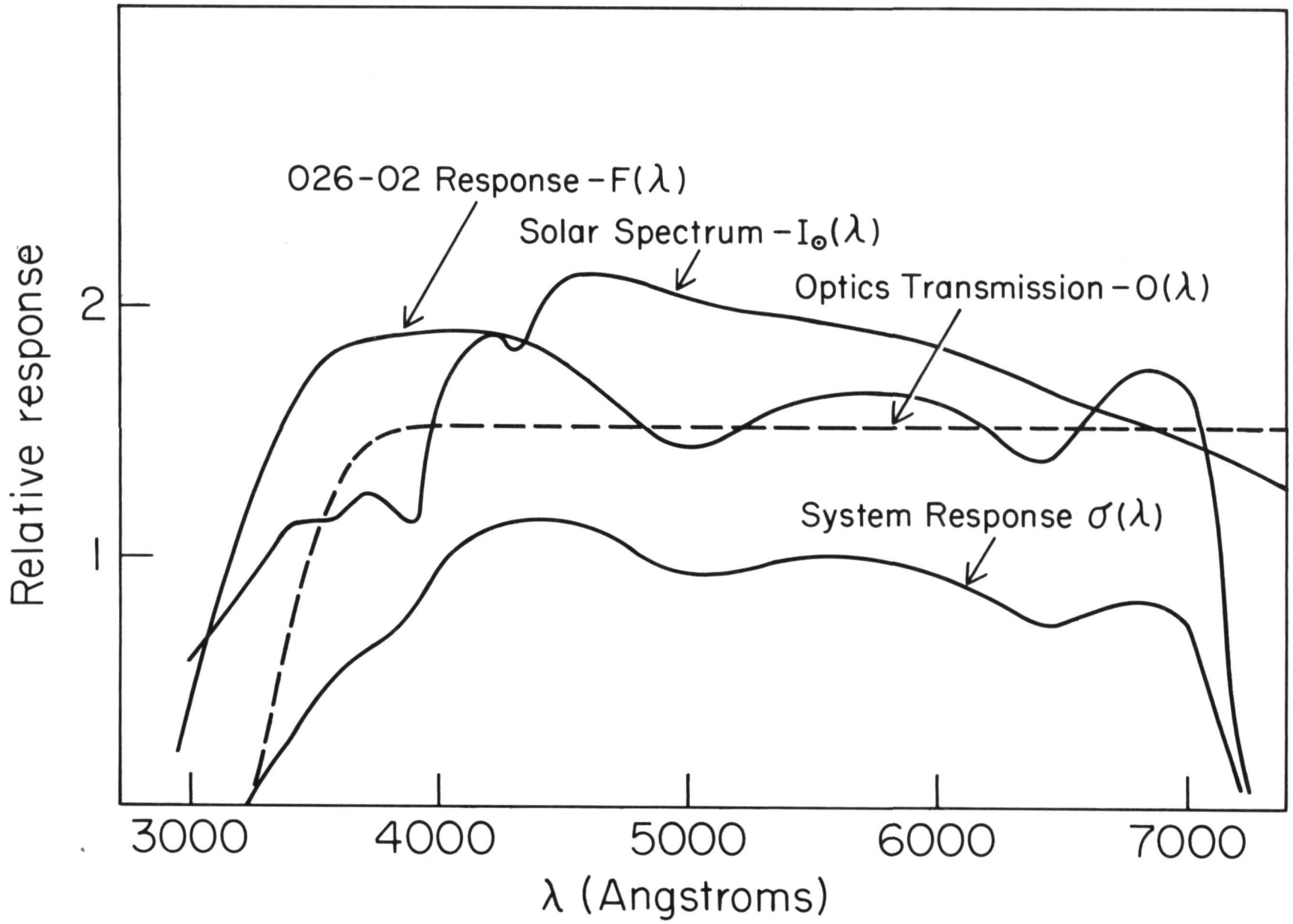

Fig. 1. The wavelength response of the S052 coronagraph.

$$E_p(\lambda) = \text{const} \cdot \underbrace{O(\lambda)}_{\substack{\text{optics}\\ \text{trans-}\\ \text{mission}}} \cdot \underbrace{F(\lambda)}_{\substack{\text{film}\\ \text{spec-}\\ \text{tral}\\ \text{response}}} \cdot \underbrace{I_p(\lambda)}_{\substack{\text{irrad.}\\ \text{of}\\ \text{particle}}} \cdot \underbrace{\pi(A/2)^2}_{\substack{\text{area of}\\ \text{aperture}}} \cdot \underbrace{\tau}_{\substack{\text{eff.}\\ \text{exp.}\\ \text{time}}} \Big/ \underbrace{\pi(a/2)^2}_{\substack{\text{area}\\ \text{on}\\ \text{film}}} . \quad (7)$$

If equation (7) is integrated over wavelength and normalized to the solar image through the same instrument, it becomes

$$W = \frac{E_p}{E_\odot} = \frac{\int I_p(\lambda)\, O(\lambda)\, F(\lambda)\, d\lambda}{\int I_\odot(\lambda)\, O(\lambda)\, F(\lambda)\, d\lambda} \cdot \frac{4 f^2 A \Omega_\odot}{a^2 T V_t} . \quad (8)$$

The results presented in a later section confirm that the particle irradiance, $I_p(\lambda)$, is due to the scattering of sunlight by particles larger than a few microns in radius. For particles of this size and larger, the scattering process is well approximated by diffraction theory (Van de Hulst, 1957):

$$I_p(\lambda) = I_\odot(\lambda) \; \frac{\rho^2 \, J_1^2 \left(\frac{2\pi\rho}{\lambda} \sin\theta\right)}{L^2 \sin^2\theta} \quad (9)$$

where ρ is radius of the particle, θ is the scattering angle, and J_1 is the first order Bessel function. Combining equations (1), (8), and (9), we find

$$W = \frac{q \, 4 \Omega_\odot}{\pi T A V_t} \quad (10)$$

where q is the system weighted average,

$$q(\rho,\theta) \equiv \frac{\int \frac{\rho^2}{\sin^2\theta} \; J_1^2 \left(\frac{2\pi\rho}{\lambda} \sin\theta\right) \sigma(\lambda)\, d\lambda}{\int \sigma(\lambda)\, d\lambda} \quad (11)$$

and $\sigma(\lambda)$ is the system response shown in Figure 1.

The function $Q = \log_{10}(q)$ is plotted in Figure 2 for various values of the particle radius, ρ. Since estimates of W and V_t can be made from the film at the various values of θ along a given track, $q(\theta)$ is also determined experimentally. By matching $\log_{10}q(\theta)$ with the curves in Figure 2, a particle size can be estimated.

There exists a region of overlap in Figure 2 in which the exact interpretation of particle size is difficult for a track which covers a narrow range of θ. The angular dependence of this effect is such that for $\theta \approx 1^{\circ}$, the photographic response from a $\rho = 10\mu m$ particle is approximately equivalent to one with $\rho = 22\mu m$, while for a smaller scattering angle of 0.5°, this degeneracy is well removed. The region of overlap shown in Figure 2 is the vestige of the oscillations of J_1^2 in the integrand of equation (11) and, because of the weight factor $\sigma(\lambda)$, is unique to the S052 coronagraph. Since the coronagraph has such a large bandpass, the averaging process (equation (11)) keeps the region of overlap to a minimum. For a narrow band instrument, the region of overlap would be much larger, and the oscillations in the individual curves of Figure 2 would be much more pronounced. It should also be noted that since only diffraction theory is employed, no information concerning the chemical composition of the particle can be obtained. On the other hand, the function Q is very sensitive to the projected geometrical cross section of the particle which, for ease of interpretation, is considered a circle of <u>radius</u> ρ.

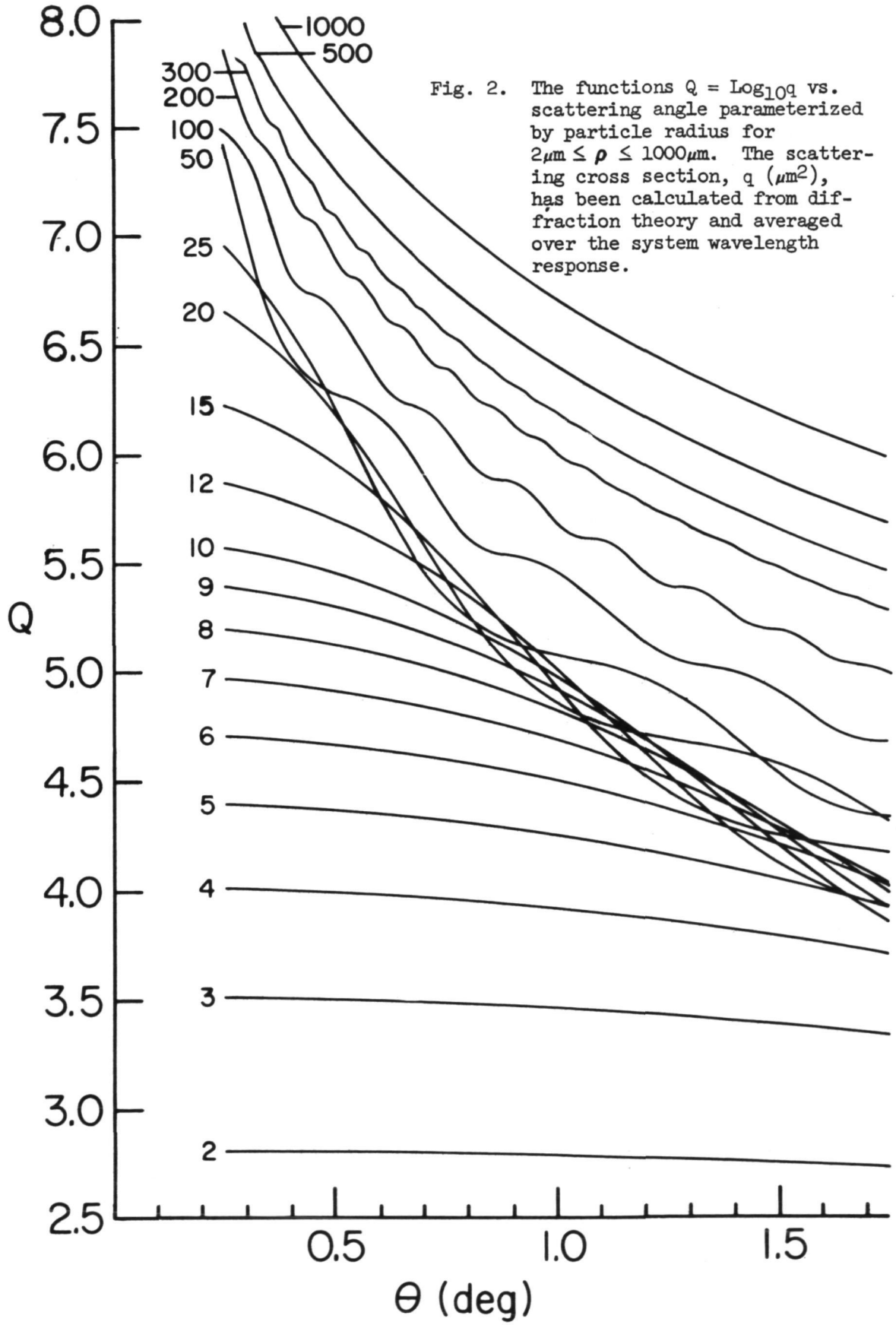

Fig. 2. The functions $Q = \mathrm{Log}_{10} q$ vs. scattering angle parameterized by particle radius for $2\mu m \leq \rho \leq 1000\mu m$. The scattering cross section, q (μm^2), has been calculated from diffraction theory and averaged over the system wavelength response.

When applying the above theory with the S052 coronagraph, the plate scale is 482 $\pm$ 3 arc-sec mm^{-1} so that the focal length, f, of the system is 428 mm. The diameter of the aperture, A, is 31.23 mm. A more complete description of the system is presented by MacQueen, et al. (1974).

The Photographic Observations and Their Reduction

The observations considered here are a sequence of pictures taken in the "continuous patrol" mode of the S052 experiment. This manually terminated mode consists of consecutive cycles of 82.5 s duration. In each cycle, 3 frames are exposed for 9, 27, and 3 s respectively. The time elapsed between the end of the 9 s exposure and the start of the 27 s exposure is 18.5 s. Between the 27 s and 3 s exposures, the elapsed time is 0.5 s. The sequence of eleven photos starts with a 3 s frame and ends with one of 27 s so that there are four 3 s frames, four 9 s frames and three 27 s frames. It was found that no tracks both started and stopped on the 27 s exposure. They were not considered further, since the locations of the track end-points are crucial to size and velocity determinations. From the eight remaining photographs, approximately 60 tracks were selected for study.

The coordinates of the two end-points of each track, along with the coordinates of a set of reference points on the film, were measured on a Mann measuring engine. The frames were then positioned in a S-3000 Specscan digital scanning densitometer, and the coordinates were reset so as to correspond with the system established when using the Mann engine. The Specscan was used to scan across the track at up to five different places. The scans were all made with a square aperture 12μm on a side. The choice of scan direction (x or y) for each track was made by choosing that axis on which the track had its shortest projection. Scans were also made of the calibration wedges in the center of each frame. All positional and

photometric data were stored on magnetic tape. A computer plot of each scan then provided a convenient format from which to infer the track width and the film densities of both the background and the track center. Also, D-Log E curves were obtained for both the 3 s and 9 s exposures by using the calibration established by Poland, et al. (1976). These curves are shown in Figure 3.

Figure 4 shows a typical working plot for extracting width and brightness. A background density and a density near the center of the track are first estimated by fitting horizontal lines at the appropriate positions. The density scale is at the left of the printout, along with other particle and frame identification data. The two densities are then converted to surface energies via the D-Log E curves. We must take into account at this point that the system has a severe, radial vignetting function whose purpose is to subdue the inner corona so as to increase the effective dynamic range of the system. This radial vignetting function is shown in Figure 5. After correcting the background and mid-track energies for vignetting, they are subtracted so that the resulting difference is the mid-track particle energy, W, used in equations (8) and (10). The track width is established by estimating the two points of the onset of the density increase. Because each data point is separated by 12μm, the width of the "bump" is determined. This width must be corrected for the fact that the scan is not necessarily perpendicular to the length of the track. When this rotation factor, which is obtained from the coordinates of the end-points of the track, is applied to this estimate, the width of the track, a, is obtained. With a and W known on

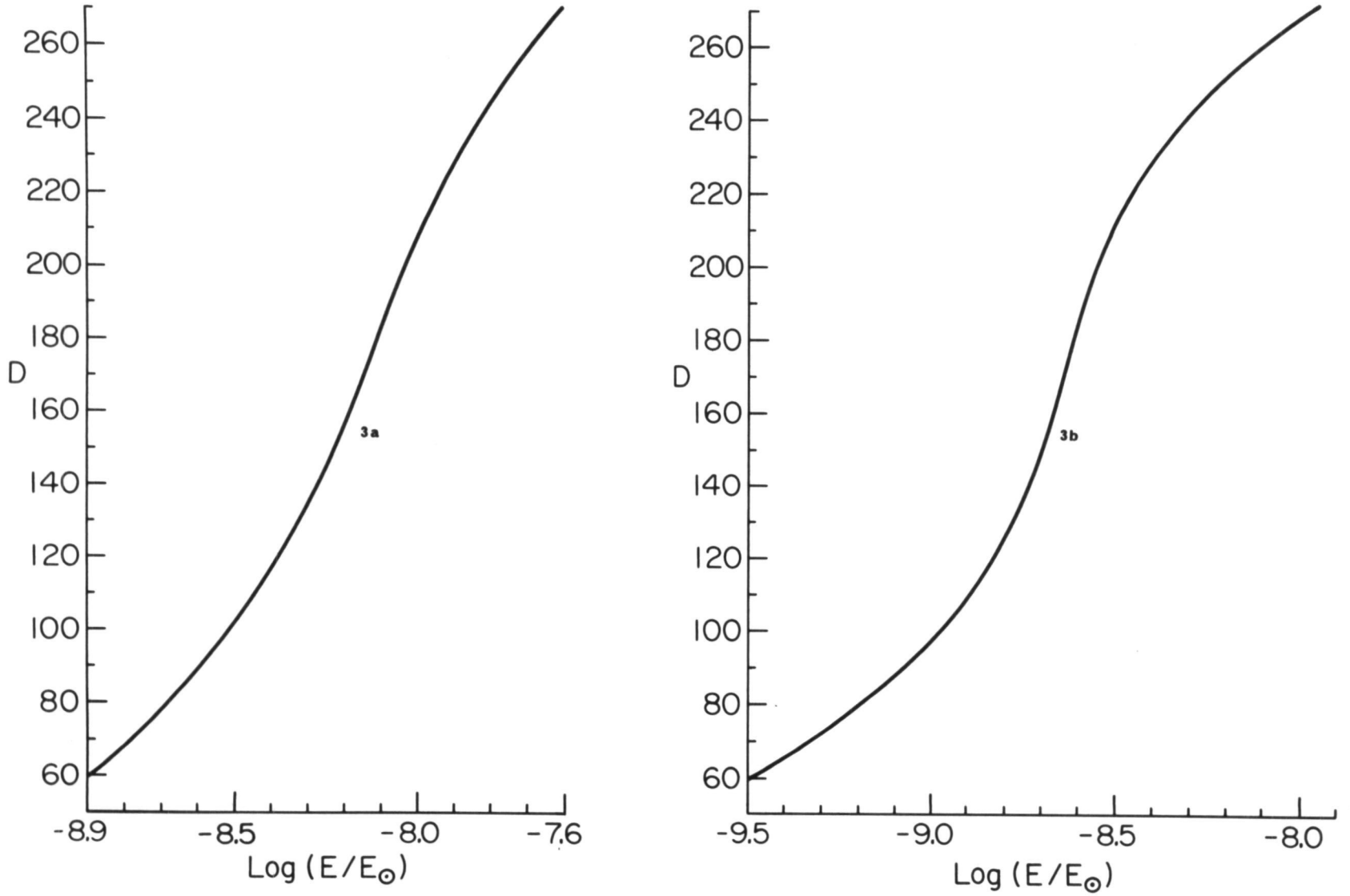

Fig. 3. Film density × 100 vs. Log (E/E_o) for 3 s exposure (3a) and 9 s exposure (3b). E_o is the rate of surface energy (ergs/cm^2 s) incident on the film due to the solar image.

Fig. 4. A typical printer plot used to obtain the width, a, of the track and the track brightness, W, above background. Scale at left is the film density times 100. Each data point is 12μm apart.

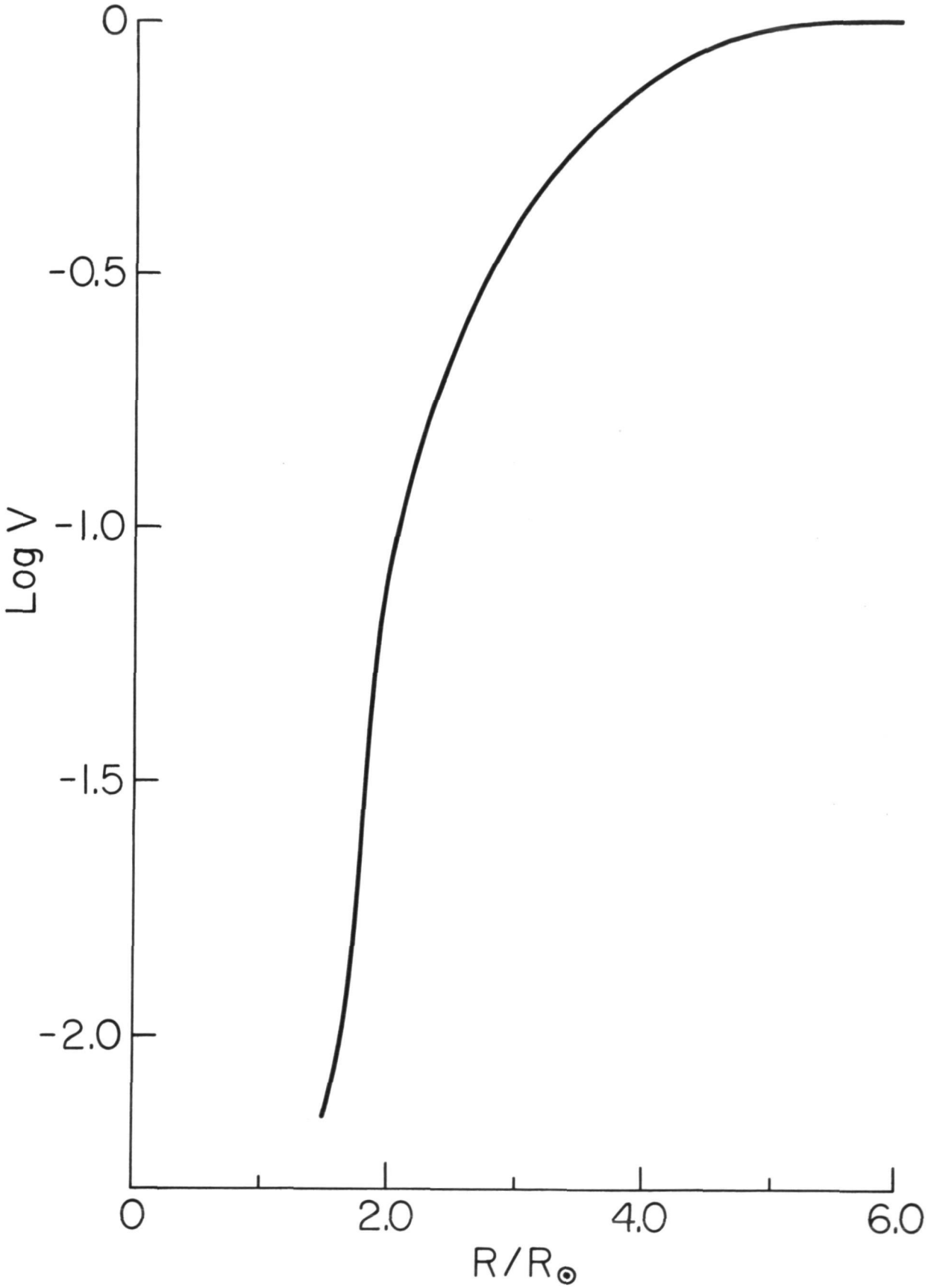

Fig. 5. The radial vignetting function. Log_{10} (transmission) is plotted vs. radial angle in units of solar radii.

at least two portions of the track, and the length of the track known as well, the theory of section II applies, and the following quantities can be determined from a single track:

(1) particle size - ρ

(2) transverse space velocity - $V_t = \sqrt{V_x^2 + V_y^2}$ (without sign)

(3) azimuthal angle of transverse velocity - $\tan^{-1}(V_y/V_x)$

(4) radial space velocity - V_r (without sign)

(5) characteristic distance of particle from spacecraft during exposure. - L

An indication of the random uncertainties in the above determinations can be found in most cases because any particular quantity has been over determined. For example, scans of the track at two points are sufficient to determine V_t and V_r. In fact, if the width of the track does not noticeably change along its length, then only one scan is needed to determine V_t, and V_r is assumed to be zero. In most cases, three scans of any track are used to determine V_t. Once V_t is established, the same three scans are used to determine three values of W so that a triplet of points is located on the scattering diagram of Figure 2. The extent to which this triplet lies along a curve of constant ρ is indicative of the uncertainty in particle radius. The measurements from any one track thus yield two or three values of V_t and ρ. The spread in these numbers, when seen in the context of a large number of particle tracks, indicates the precision in which ρ and V_t can be determined. The same method is used for determining the uncertainty in V_r and L.

The ρ, V_t plane makes a convenient format for the discussion

and presentation of the results for each track. Not only can ρ and V_t and their associated errors be plotted in this plane, but the limit of particle detectability can also be represented by this scheme. This is because q (ρ,θ) is proportional to WTV_t as shown in equation (10). At a fixed value of θ, the quantity WT has a minimum value, $(WT)_{min}$, below which no track can be distinguished. This minimum value is influenced by the vignetting function shown in Figure 5, and therefore depends upon radial position in the focal plane. However, $(WT)_{min}$ is rather insensitive to the exposure time T. This is because W is the energy due to the track above background. Since the background increases with exposure time, the actual value of W decreases with increasing T. The quantity $(WT)_{min}$, however, is found to be about the same for both the 3 s and 9 s exposures - $(WT)_{min} = \frac{9 \times 10^{-10}}{V(\theta)}$ s. By setting $WT = (WT)_{min}$ in equation (10), detectability limits can be established in the ρ, V_t plane for fixed values of the scattering angle. These limits, parameterized by θ, are shown in Figure 6. We define the "system limit" to be the bottom envelope of these curves.

The eight photographs studied, along with the results, are shown on the following pages. The photographs themselves are labelled by 2 numbers. The first digit, which ranges from 1 to 4, designates the time order of the photographs, and the second digit refers to the exposure time (3 or 9 secs). The tracks considered are identified on the photograph by letters. Each photo is accompanied on its reverse side by the scattering diagram from which the particle sizes for each track have been found. These are followed by a summary plot (Figure 7) of all points in

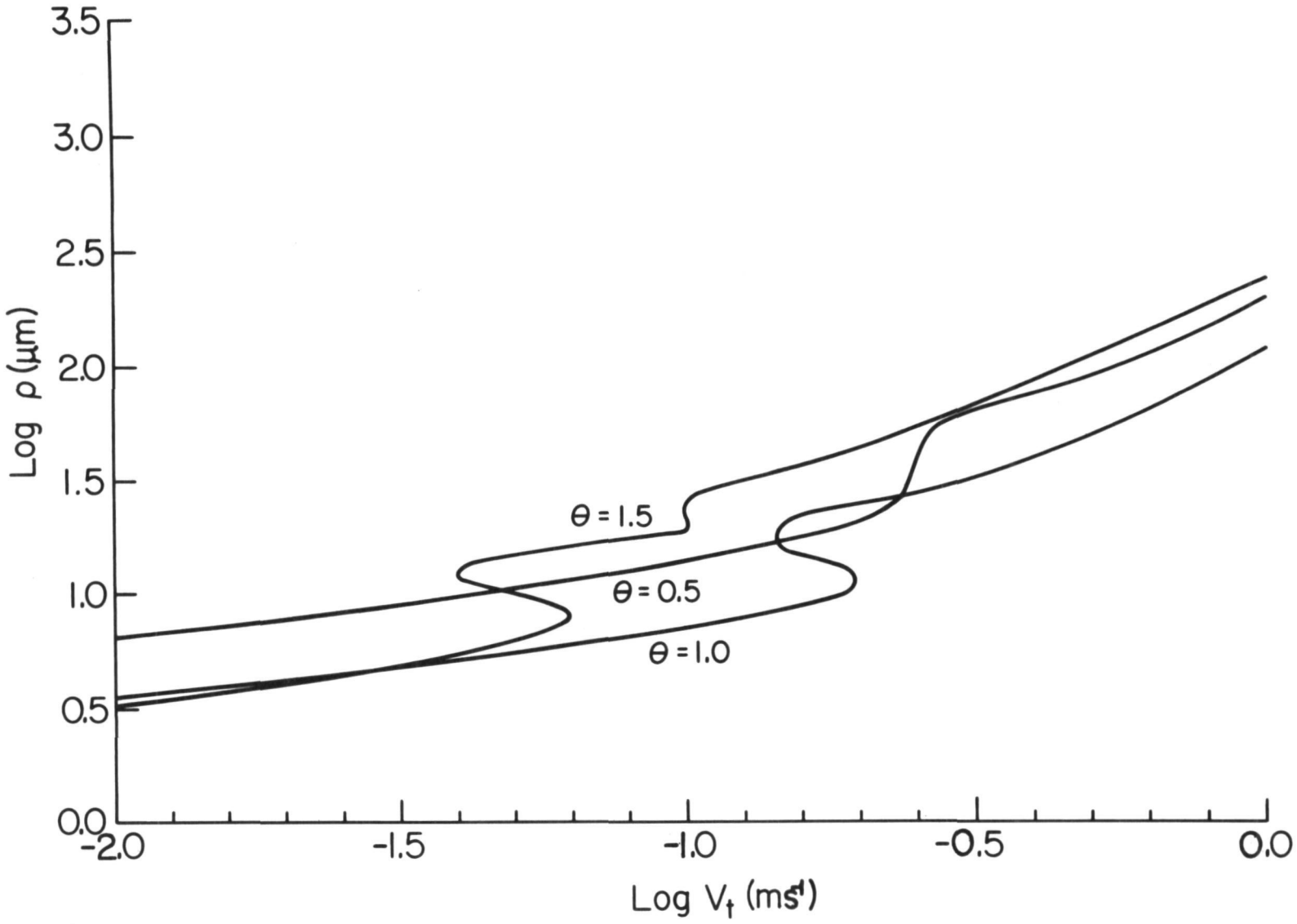

Fig. 6. The detectability limits for three scattering angles. Any particle below the curves in the ρ, V_t plane will not be detected by the system.

This page intentionally blank

1-3

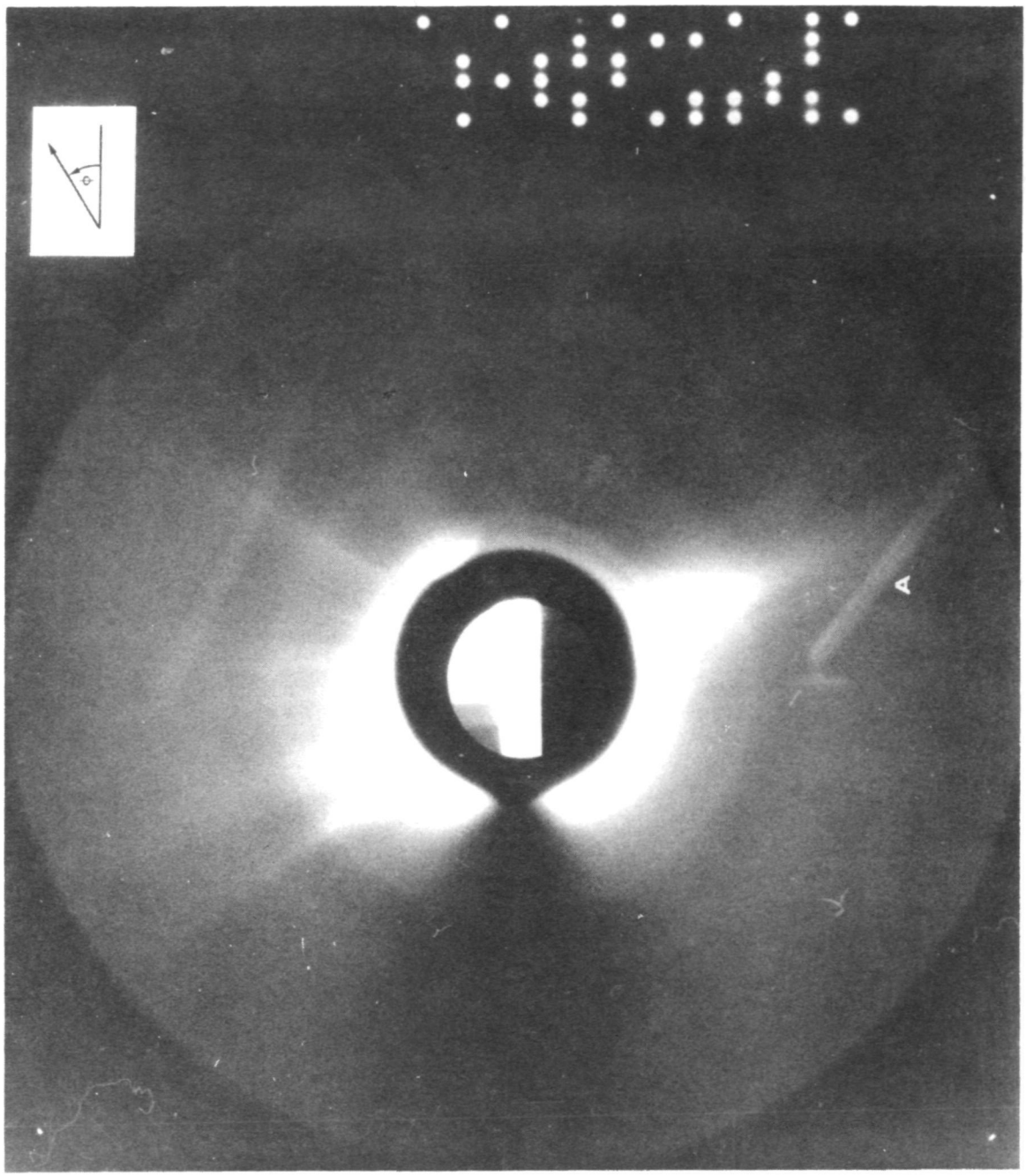

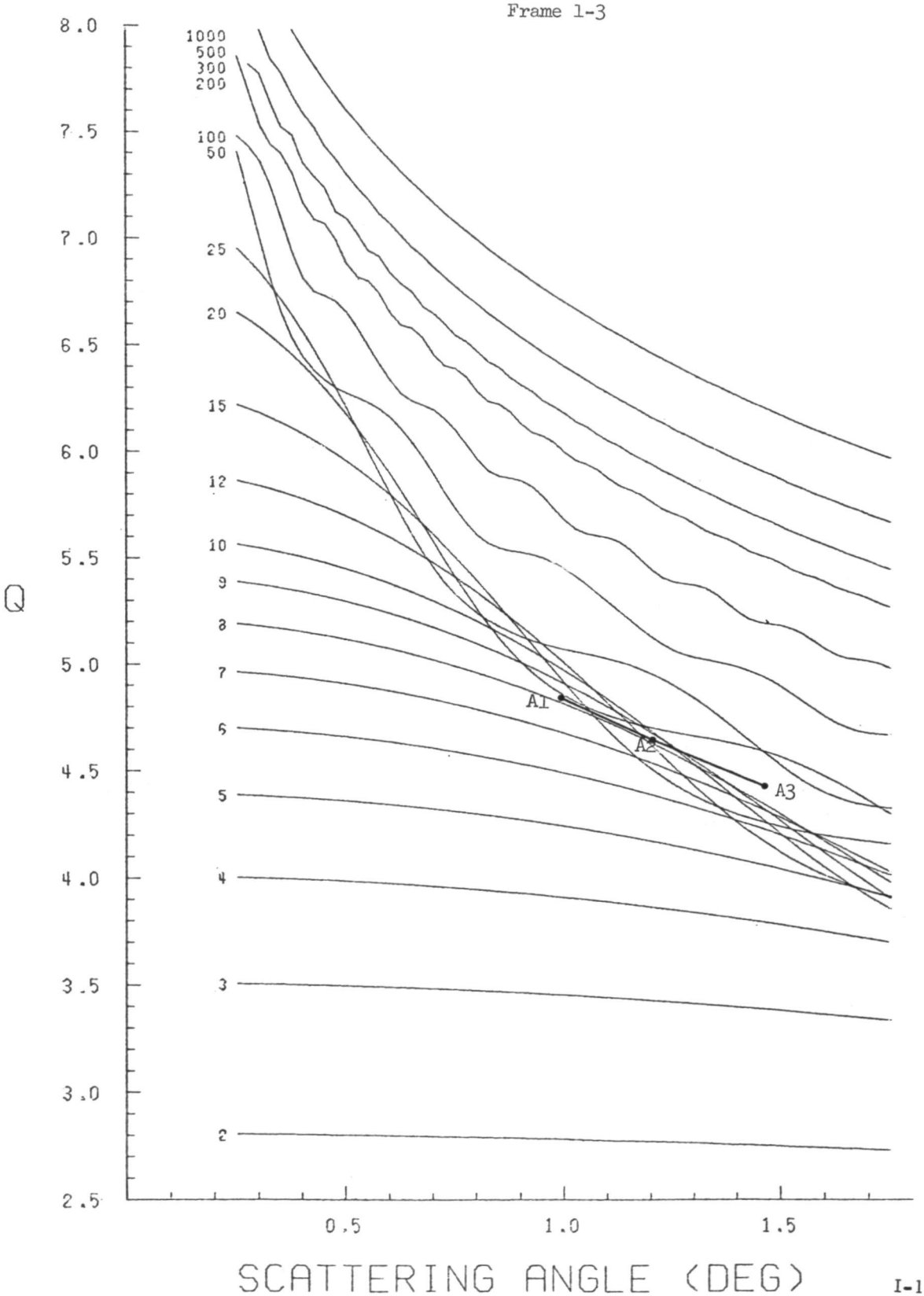
8.0
7.5
7.0
6.5
6.0
5.5
5.0
4.5
4.0
3.5
3.0
2.5
Q
1000
500
300
200
100
50
25
20
15
12
10
9
8
7
6
5
4
3
2
A1
A2
A3
0.5
1.0
1.5
SCATTERING ANGLE (DEG)

1-9
F
G
C
D
H
K

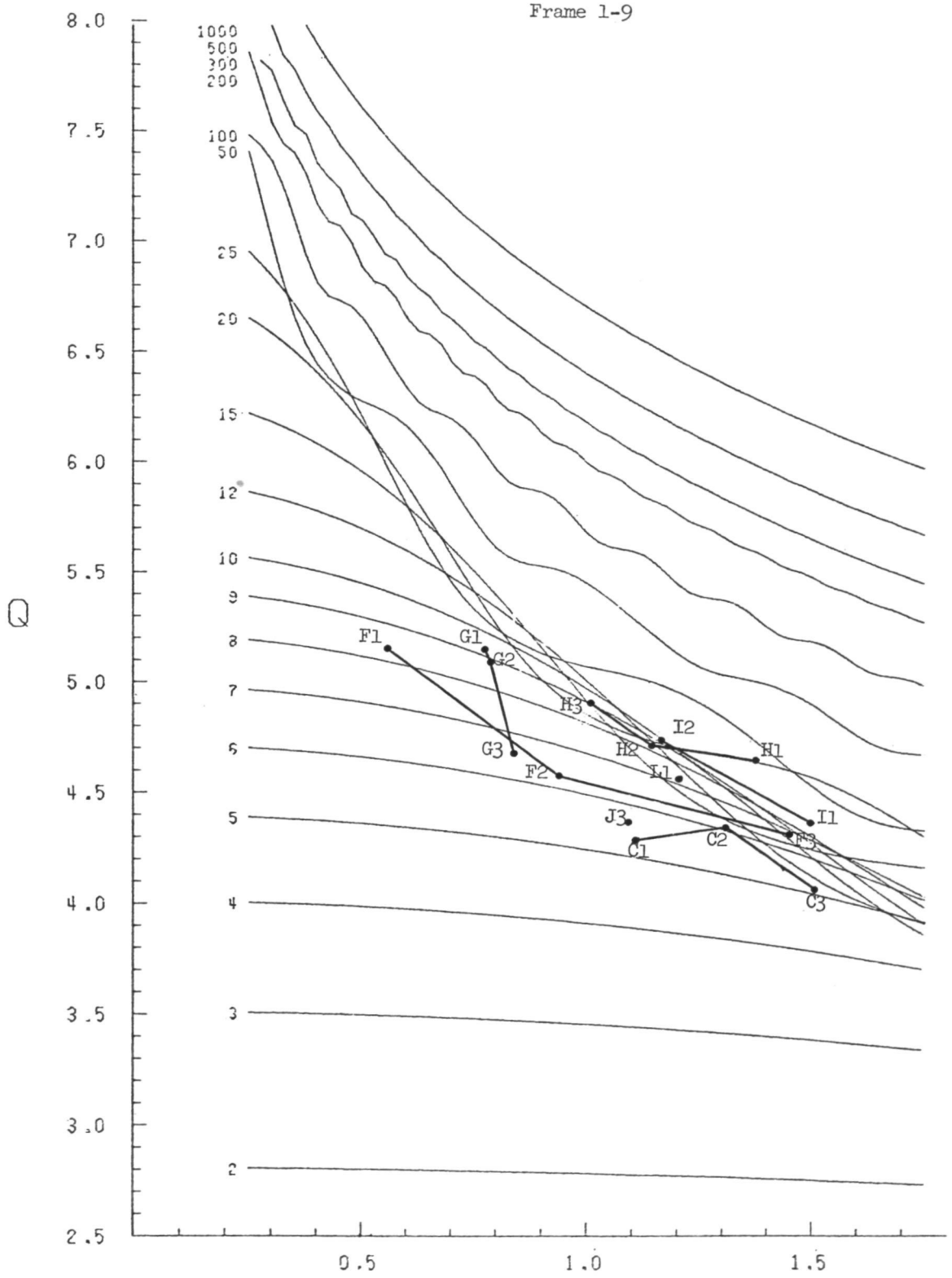
8.0
7.5
7.0
6.5
6.0
5.5
5.0
4.5
4.0
3.5
3.0
2.5
Q
1000
500
300
200
100
50
25
20
15
12
10
9
8
7
6
5
4
3
2
F1
G1
G2
G3
F2
H3
H2
H1
I2
I1
J3
C1
C2
C3
0.5
1.0
1.5
SCATTERING ANGLE (DEG)

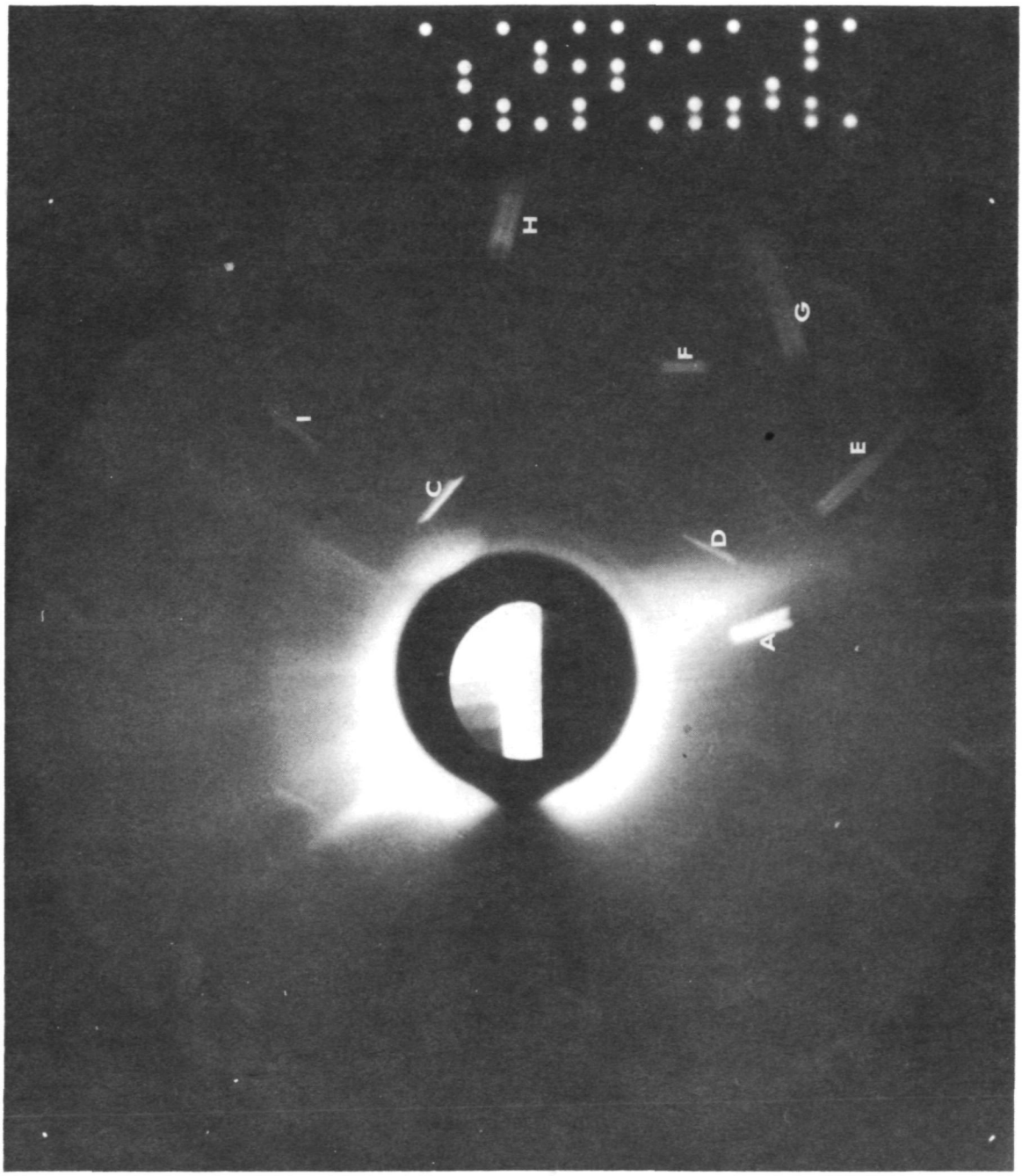
2-3
H
G
F
I
C
E
D
A

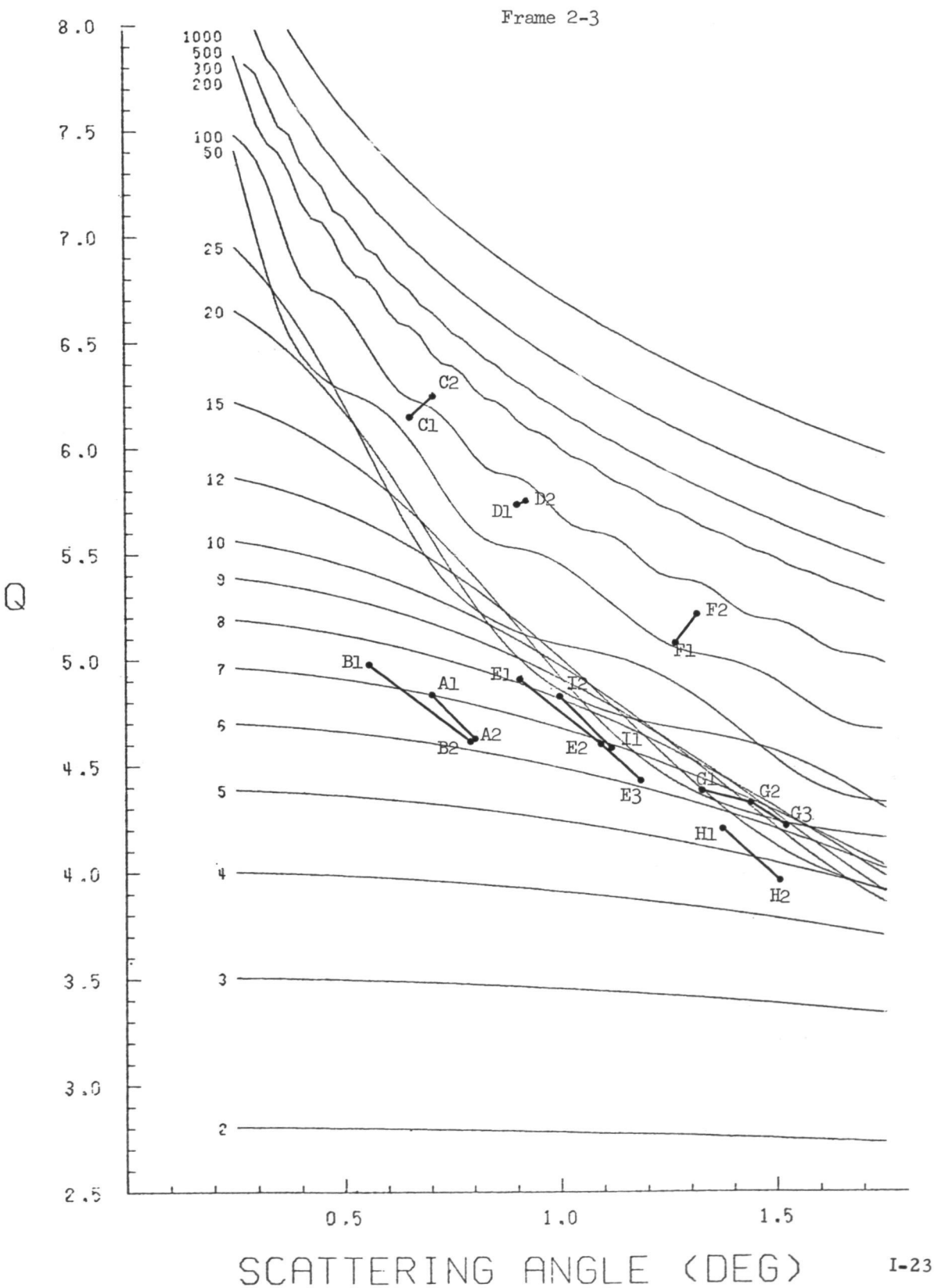
Frame 2-3
8.0
7.5
7.0
6.5
6.0
5.5
5.0
4.5
4.0
3.5
3.0
2.5
Q
1000
500
300
200
100
50
25
20
15
12
10
9
8
7
6
5
4
3
2
C2
C1
D1
D2
F2
F1
B1
A1
A2
B2
E1
I2
E2
I1
E3
G1
G2
G3
H1
H2
0.5
1.0
1.5
SCATTERING ANGLE (DEG)

2-9
Z
BB
AA
W
X
V
Y
K

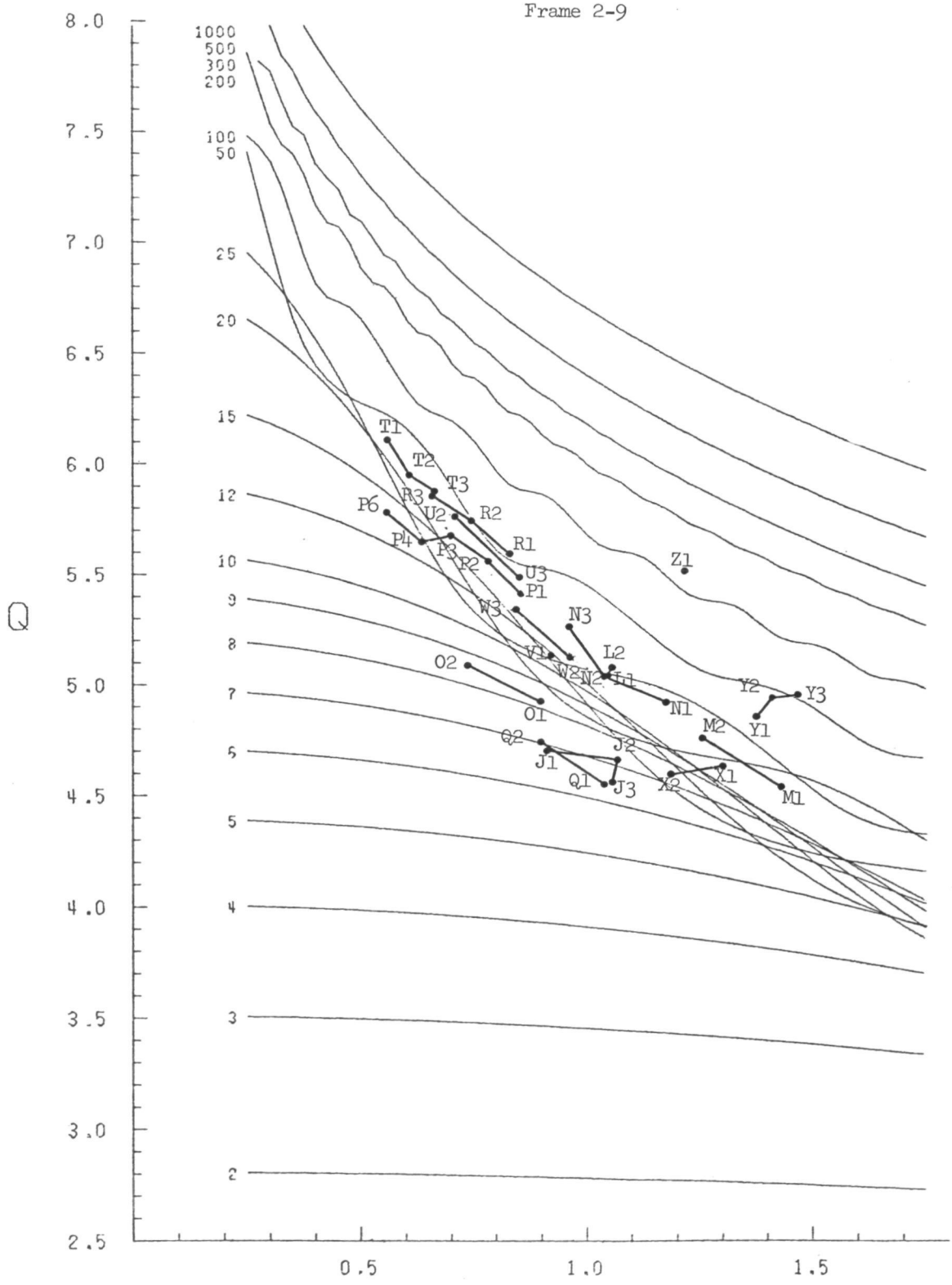
8.0
7.5
7.0
6.5
6.0
5.5
5.0
4.5
4.0
3.5
3.0
2.5
Q
1000
500
300
200
100
50
25
20
15
12
10
9
8
7
6
5
4
3
2
T1
T2
T3
R3
P6
U2
R2
P4
P3
P2
R1
U3
P1
W3
N3
V1
W2
N2
L2
J1
O2
O1
Q2
J2
Q1
J3
N1
Z1
Y2
Y3
Y1
M2
X2
X1
M1
0.5
1.0
1.5
SCATTERING ANGLE (DEG)

3-3
A
B
C
D
E
F
G

Frame 3-3

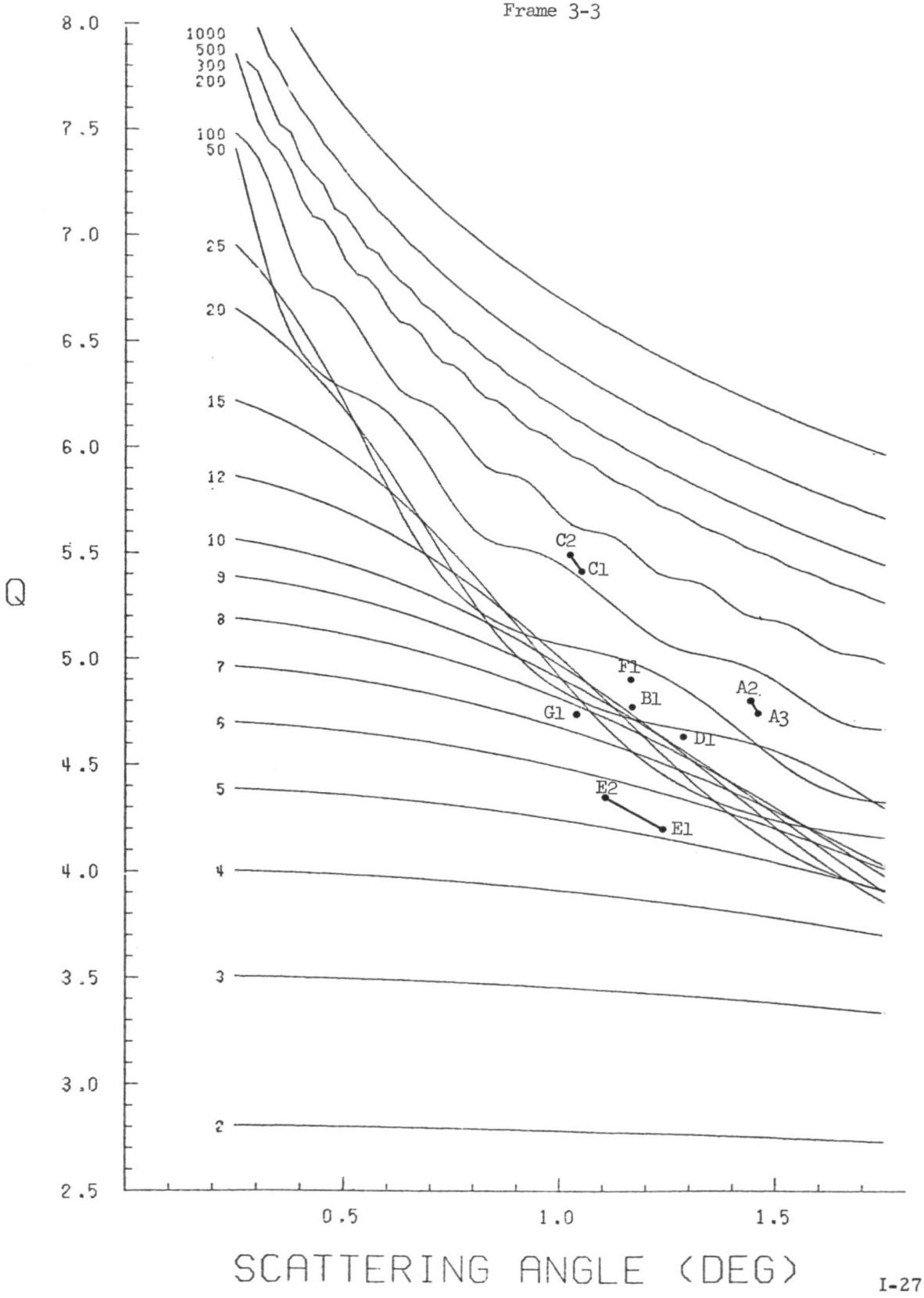
8.0
7.5
7.0
6.5
6.0
5.5
5.0
4.5
4.0
3.5
3.0
2.5
Q
1000
500
300
200
100
50
25
20
15
12
10
9
8
7
6
5
4
3
2
C2
C1
F1
B1
G1
A2
A3
D1
E2
E1
0.5
1.0
1.5
SCATTERING ANGLE (DEG)

3-9
P
Q
H
I
N
O
R
M
T
K
J
L

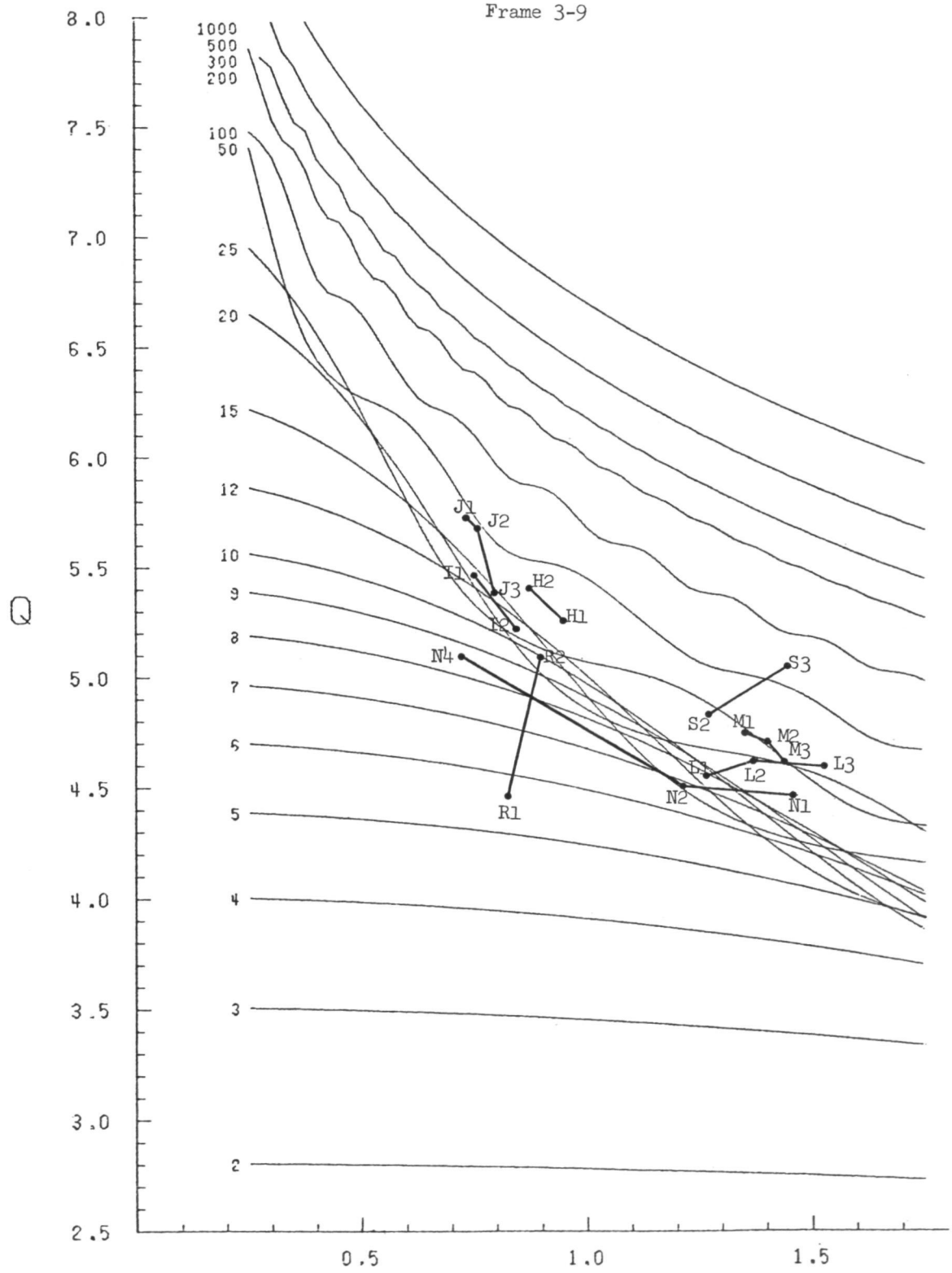
8.0
7.5
7.0
6.5
6.0
5.5
5.0
4.5
4.0
3.5
3.0
2.5
Q
1000
500
300
200
100
50
25
20
15
12
10
9
8
7
6
5
4
3
2
J1
J2
I1
J3
H2
H1
I2
N4
R2
S3
S2
M1
M2
M3
L3
L2
L1
N2
N1
R1
0.5
1.0
1.5
SCATTERING ANGLE (DEG)

4-3
C
A
D

Frame 4-3

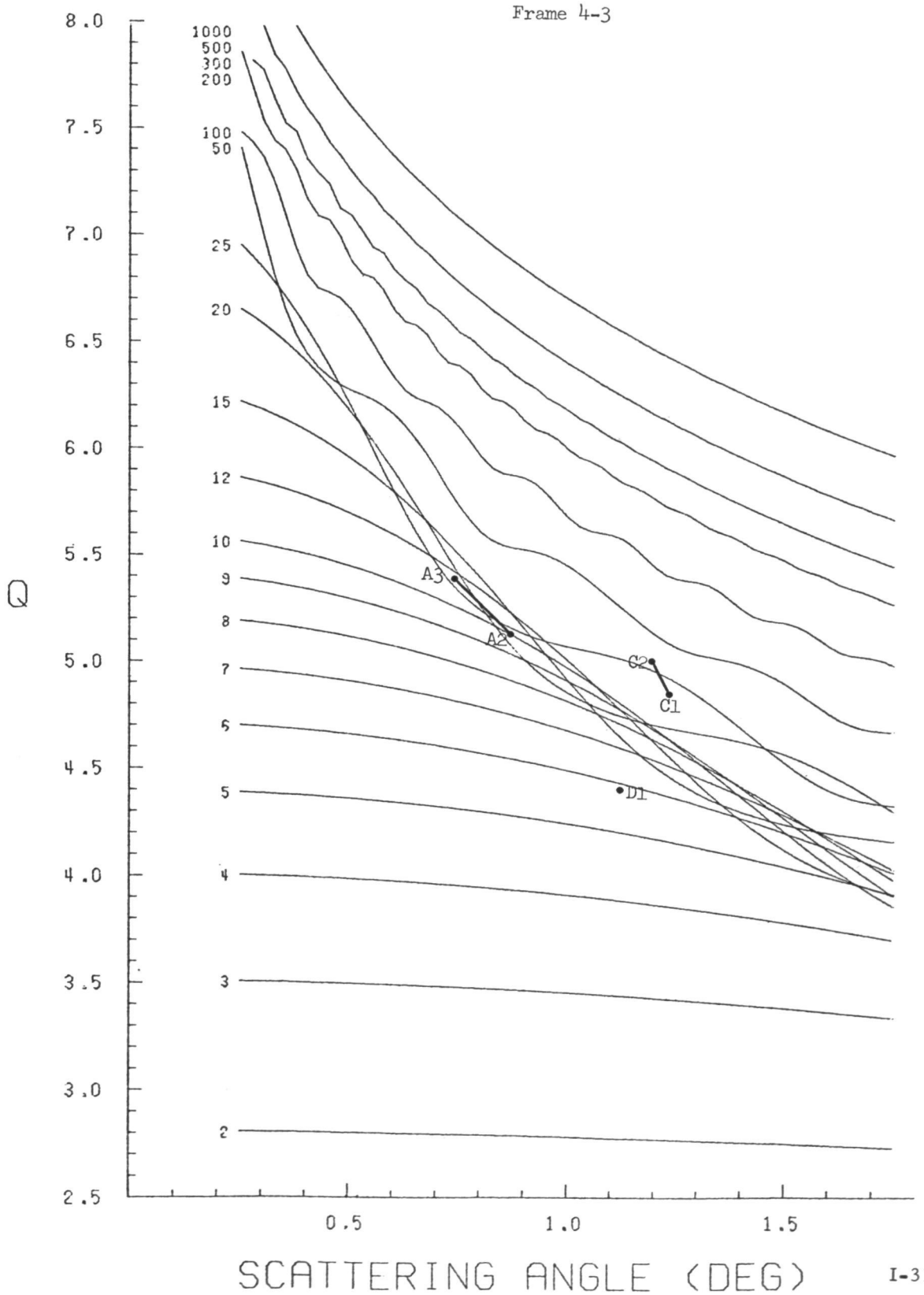
8.0
7.5
7.0
6.5
6.0
5.5
5.0
4.5
4.0
3.5
3.0
2.5
Q
1000
500
300
200
100
50
25
20
15
12
10
9
8
7
6
5
4
3
2
A3
A2
C2
C1
D1
0.5
1.0
1.5
SCATTERING ANGLE (DEG)

4-9

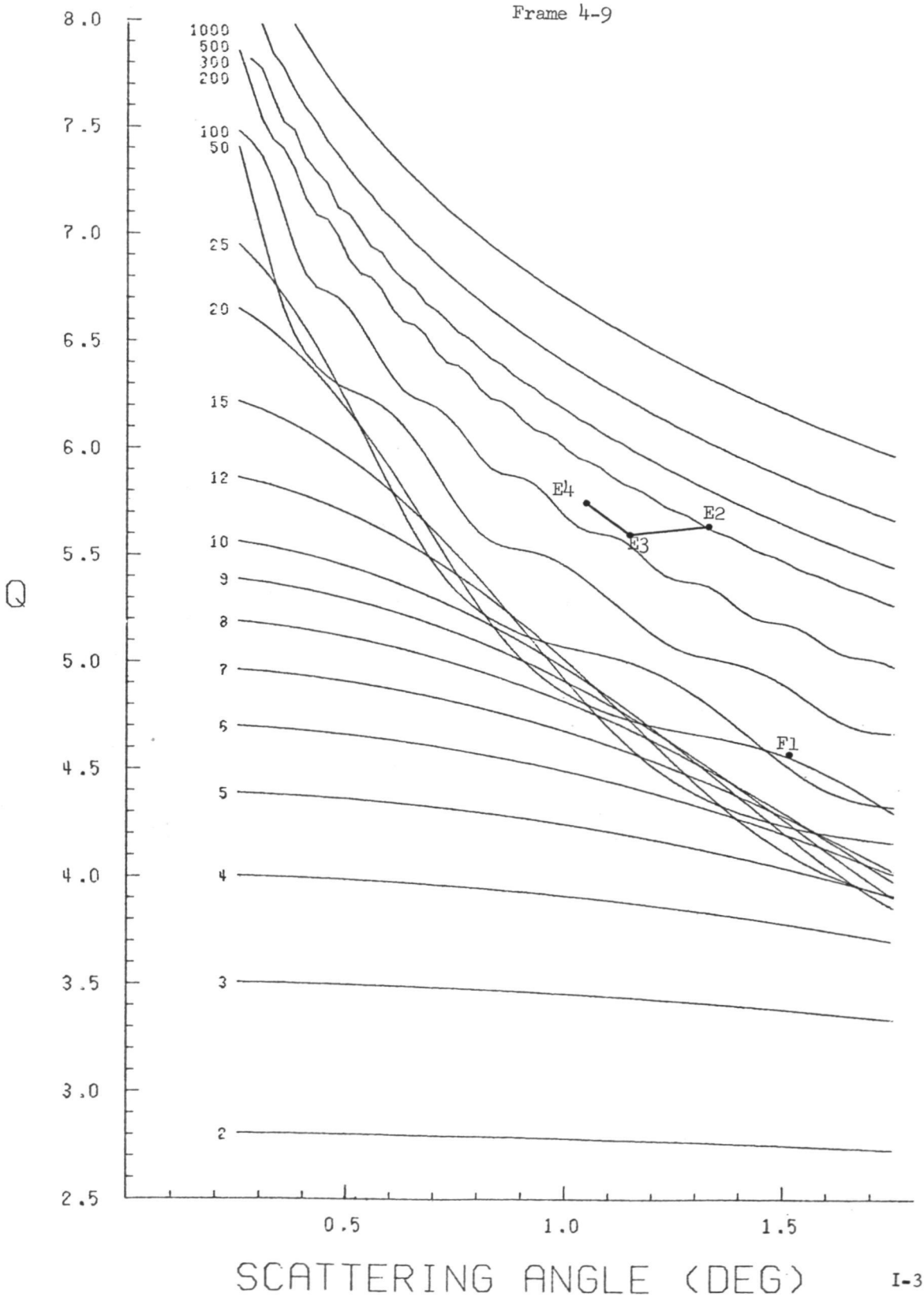
8.0
7.5
7.0
6.5
6.0
5.5
5.0
4.5
4.0
3.5
3.0
2.5
Q
1000
500
300
200
100
50
25
20
15
12
10
9
8
7
6
5
4
3
2
E4
E2
E3
F1
0.5
1.0
1.5
SCATTERING ANGLE (DEG)

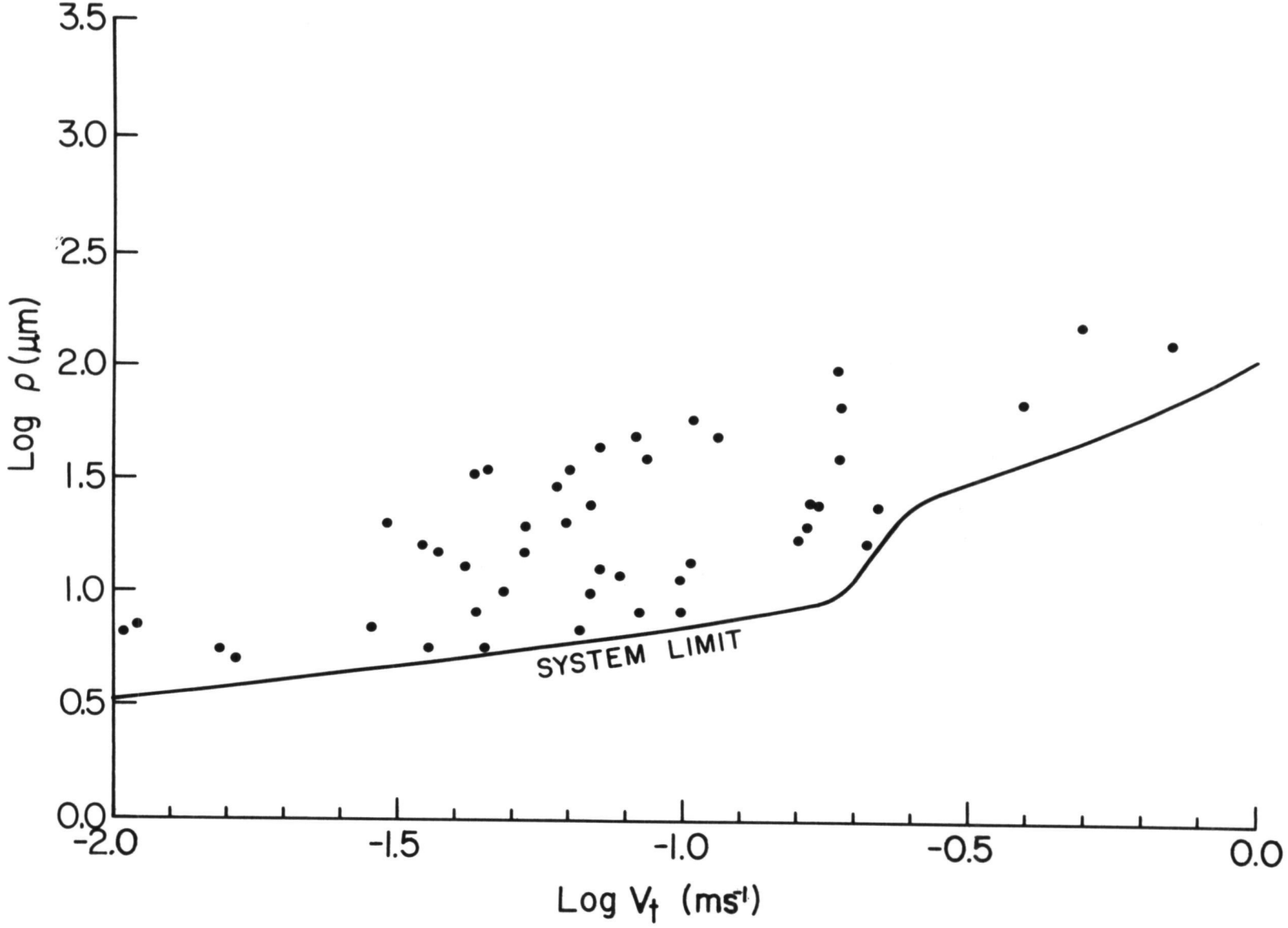

Fig. 7. Plot of photographic results. All of the particles are shown in the ρ, V_t plane along with the system limit.

the log ρ, log V_t plane along with the system limit. It is evident that the bottom of the distribution of points is interrupted by the system limit. The distribution itself undoubtedly continues downward to include particles smaller than the system can detect. On the other hand, if particles larger than 100μm truly are present, they should be observable. Because of this, we interpret the upper cutoff of particle sizes to be a real effect and representative of the spacecraft environment at the time the pictures were taken. The upper bound on V_t, on the other hand, arises because of the restriction that a particle image must both start and stop on the frame. It does not represent the true velocity limit of the contamination cloud.

A summary of all the inferred parameters is presented in Table 1. In some cases, either a densitometer scan was positioned incorrectly on the track, or the track was not distinguishable above the background so that some of the parameters could not be determined. These cases are represented by dashes in the appropriate columns of Table 1. In that table, the frames are presented in chronological order along with the track designation. The average radial velocity of each particle is presented in the next column along with its standard deviation if two or more determinations of V_r were made. The next column contains the range of particle distances as determined from measurements of the track width. The next two columns specify the transverse velocity. The column marked V_t gives the magnitude and its standard deviation (where possible) and the column labelled ϕ gives the track direction as seen on the photograph. The definition of ϕ is provided by the inset in the photograph 1-3. Since there is

Table 1

PHOTOGRAPHIC RESULTS

Frame	Track	V_r Radial velocity in $m\text{-}s^{-1}$	L Distance in m	V_t, Transverse velocity in $m\text{-}s^{-1}$	ϕ Track angle in deg	ρ Particle radius in μm lower limit	best estimate	upper limit
1-3	A	4.5 ± 5.2	30-40	0.133 ± .023	141	8	12	18
1-9	D	0.8 ± ---	16-24	0.051 ± ----	143	--	--	--
	C	0.7 ± 0.5	23-28	0.015 ± .011	91	5	6	6
	F	1.7 ± 1.5	19-31	0.028 ± .011	155	6	7	8
	G	2.3 ± 6.0	37-49	0.080 ± .022	105	6	8	10
	H	0.6 ± 3.3	21-30	0.053 ± .048	150	8	15	25
	I	0.6 ± ---	21-25	0.037 ± ----	141	9	15	17
	L	1.7 ± 4.7	35-42	0.077 ± .051	120	7	12	17
	J	0.8 ± 1.5	23-35	0.045 ± .038	90	--	6	--
2-3	A	2.6 ± ---	31-36	0.007 ± ----	109	6	7	7
	B	4.4 ± ---	40-62	0.011 ± ----	92	6	7	8
	C	19.6 ± ---	64-90	0.188 ± ----	137	70	100	130
	D	25.6 ± ---	84-126	0.392 ± ----	62	60	70	80
	E	0.9 ± 0.8	32-35	0.069 ± .012	134	6	10	20
	F	7.4 ± ---	34-44	0.192 ± ----	88	50	65	80
	G	1.3 ± 1.3	19-22	0.048 ± .009	17	6	10	15
	H	0.9 ± ---	22-24	0.016 ± ----	165	5	5	6
	I	1.5 ± ---	58-60	0.101 ± ----	50	7	12	20
2-9	J	2.2 ± 3.8	69-85	0.065 ± .025	50	6	7	12
	M	0.4 ± ---	43-45	0.035 ± ----	87	10	16	27
	L	5.0 ± 13.	105-136	0.166 ± .042	45	13	20	26
	N	0.0 ± ---	*246-247	*0.220 ± ----	46	23	25	30
	O	1.4 ± ---	38-46	0.043 ± ----	65	8	8	8
	Q	1.2 ± ---	27-33	0.010 ± ----	88	6	7	7
	T	5.2 ± 1.4	25-57	0.043 ± .018	154	25	35	45
	P	7.3 ± 18.	39-98	0.062 ± .073	72	13	21	35
	R	1.4 ± 13.	35-113	0.116 ± .065	68	40	50	55
	U	11.3 ± 13.	42-128	0.190 ± .127	66	35	40	45
	V	1.7 ± 9.7	56-118	0.162 ± .033	55	12	18	25
	W	4.8 ± 4.6	75-115	0.173 ± .088	45	15	25	35
	Z	31.0 ± 89.	78-140	0.717 ± 1.080	43	--	130	--
	BB	---	96	0.101 ± ----	37	--	--	--
	AA	3.3 ± ---	121-151	0.317 ± ----	61	--	--	--
	X	3.2 ± 8.5	53-88	0.072 ± .018	49	7	13	20
	Y	1.4 ± 4.8	29-44	0.071 ± .049	69	35	45	55
3-3	B	---	50	---	52	10	15	21
	C	8.4 ± ---	119-131	0.146 ± ----	45	50	60	70
	A	1.4 ± 4.0	17-20	0.063 ± .024	139	30	35	40
	D	---	44	---	50	12	17	25
	E	21.1 ± ---	38-41	0.035 ± ----	61	5	6	6
	G	---	89	---	51	7	15	20

* Probably a lower limit.

Table 1

continued

Frame	Track	V_r Radial velocity in $m\text{-}s^{-1}$	L Distance in m	V_t Transverse velocity in $m\text{-}s^{-1}$	ϕ Track angle in deg	ρ Particle radius in μm lower limit	best estimate	upper limit
3-3	F	---	63	----	55	--	23	--
3-9	K	0.3 ± ---	88-91	0.063 ± ----	68	--	--	--
	H	0.5 ± ---	72-74	0.045 ± ----	54	30	35	40
	J	5.3 ± 0.2	68-101	0.086 ± .006	53	12	40	50
	I	1.0 ± ---	113-119	0.053 ± ----	51	10	20	25
	L	0.7 ± 0.4	67-71	0.030 ± .011	45	8	20	25
	M	2.2 ± 5.4	25-39	0.069 ± .000	53	20	25	25
	N	0.2 ± 4.0	29-47	0.042 ± .006	48	7	13	18
	O	---	258	0.344 ± ----	43	--	--	--
	P	5.0 ± ---	36-82	0.232 ± ----	40	--	--	--
	Q	7.5 ± ---	133-201	0.202 ± ----	41	--	--	--
	R	5.9 ± ---	153-184	0.098 ± ----	42	5	8	22
	T	---	*225	*0.162 ± ----	51	--	--	--
	S	0.3 ± 5.0	30-50	0.082 ± .061	54	25	50	75
4-3	D	---	70	----	56	--	6	--
	C	5.1 ± ---	92-100	0.171 ± ----	44	23	28	30
	A	5.2 ± 6.5	37-50	0.213 ± .118	23	10	17	25
4-9	F	---	90	0.059 ± ----	43	--	30	--
	E	0.5 ± 20.	54-163	0.488 ± .177	54	120	120	200
	G	---	74	0.058 ± ----	43	--	--	--
Average		4.5		0.122			27	
Average error		8.9		0.083				

* Probably a lower limit.

no way to tell the sign of the direction of the particle, the range of angle is limited to $0<\phi<180$.

The last 3 columns provide the best estimate of upper and lower bounds to the particle size. These are inferred from the scattering diagrams presented with each photo. The average particle size as determined from the best estimate column is 27μm. Since the sample is biased at least by the system limit, this number represents only an upper limit on the average of the true distribution.

The Video Tape Investigation

A very convenient feature of the video tape provided to us is that it has been modified so that the GMT, in one second intervals, is displayed in the center of the frame. This provides a way of labeling particles as well as measuring time intervals for velocity estimates. The various segments of the tape are summarized in Table 2. Two of those segments were selected for analysis: days 166 and 220.

Day 166 is of the utmost importance due to the presence of Saturn in the field of view. Because the video mode does not include the step-wedge calibration image, Saturn offers the best available means for a photometric calibration. Also, the plate scale for the video mode is different for the x and y directions as is obvious from the elliptical appearance of the occulting disk. Since the instrument is rotated approximately 90° during the day 166 tape segment, a continuous set of data is available to determine these two scale factors by using Saturn's known elongation of 1.10°.

Day 220 was chosen to be analyzed because this segment offers a wide variety of particle speeds and image sizes. The random directions of motion indicate that the particles are probably not associated with a dump, and they might therefore be more representative of the ambient environment.

The exposure time of the video system is 1/60 s, so that, at any instant, most particle images are not tracks as on the photographs, but rather well-defined circles-of-confusion. The diameter of the

Table 2

SAMPLE S052 VIDEO TAPE - SUMMARY OF SEGMENTS

Day of Year - GMT	Duration	Contents and Comments
----	60 s	Bar pattern
166-15:02:36	76 s	Saturn in field of view with an elongation angle of 1.103° and magnitude m_V = +0.3. Instrument shown rotating through 90°. No contamination.
220-17:34:06	340 s	Moderate contamination from all directions. Decreases in time. Good variety.
240-10:36:30	82 s	No contamination at start. At 37:00, violent snowstorm - highly directional. Very likely associated with a dump. Time decay evident.
249-06:33:15	185 s	No contamination at start. Instrument shown rotating and returning to original position. A few particles at 35:54. Close one at 36:00.
Bad GMT (clock not running)	87 s	Few particles. Very slow.
----	110 s	Bar pattern

circle, a, the x and y video positions, the brightness/area, h, and the time were all measured at three points along the path of the particle's image. In practice, the y coordinate was obtained from a grid placed directly over the TV screen after the monitor had been adjusted for vertical linearity. The x, a, and h measurements were read from an oscilliscope monitoring the video signal. By suitable delaying techniques, the single line of interest was displayed. The x position was recorded as the time from the start of the line to the center of the image, and a was similarly obtained as the time required to sweep the particle image. Possible non-linearities in the monitor sweep were thus avoided. Furthermore, the amplitude (h) of the particle's video signal above background could be read directly from the scope. Here it was assumed that the amplitude response of the system was linear. The observation of Saturn made it possible to convert the positional parameters x, y, and a to arc degrees and the brightness of the particle image to units of the sun's surface brightness.

The reduction of the video data differs from that of the photographic data in two important respects. First, the particles that can be fully investigated are not limited to the extent that they were in the photographic method, where the particle had to both start and stop on the film. In the video method, we only require that the image speed be small enough so that the image itself registers as circular within any individual frame. In effect, about 95% of all particles observable on the tape fulfill this criteria. Second, the theory developed in an earlier section needs certain modifications.

In particular, the "effective" exposure time, τ, is no longer a defined quantity and Δt, formerly defined by equation (3), is now just the time interval between two consecutive measurements. Finally, equations (7) and (8) must be redeveloped with τ being replaced by T so that equation (10) is replaced by the expression

$$W = \frac{4\, q\, \Omega_{\odot}}{\pi A^2} = \frac{h}{V(\theta)}, \tag{12}$$

where $V(\theta)$ is the vignetting function. This reduces to

$$Q = \log_{10}(q) = 4.61 + \log h - \log V(\theta) \tag{13}$$

where h = 1 corresponds to 3.6×10^{-9} sun surface brightness and the range of h (assumed linear) is about 0.2 to 4.0.

Video System Limits and Restrictions

For rigor, the wavelength response of the SEC video tube should be used in place of the film response in equation (7). Not having immediate access to that response function, we assume in what follows that the SEC and the film have similar characteristics so that the scattering diagram used in the photographic method can also be used here. However, it is interesting to note that Q is not a function of V_t as in the photographic mode. Using a minimum detectable value of 0.2 for h we can generate, as in Figure 8, minimum values for Q as a function of scattering angle. From this figure, the smallest particle size that is detectable in the video mode can be obtained. In a similar manner, another curve can be generated for h = 4.0. Particles corresponding to points above this curve produce a signal which saturates the system, and only a lower limit can be placed on the particle size. Of the 34 particles studied by this method, only 1 was near the saturation limit.

Limits on the largest velocity that can be inferred from the video method have been determined from practical experience. Particles which have an angular velocity, $\dot{\omega}$, larger than about $7^{o}\ s^{-1}$ begin to smear out on any single video frame. The image is no longer circular and photometric measurements become difficult. The conversion of angular velocity to transverse space velocity V_t is given by

$$\dot{\omega}\ (\text{arc - deg}\ s^{-1}) = .0573\ \frac{V_t\ (\text{mm}\ s^{-1})}{L\ (\text{m})}\ , \qquad (14)$$

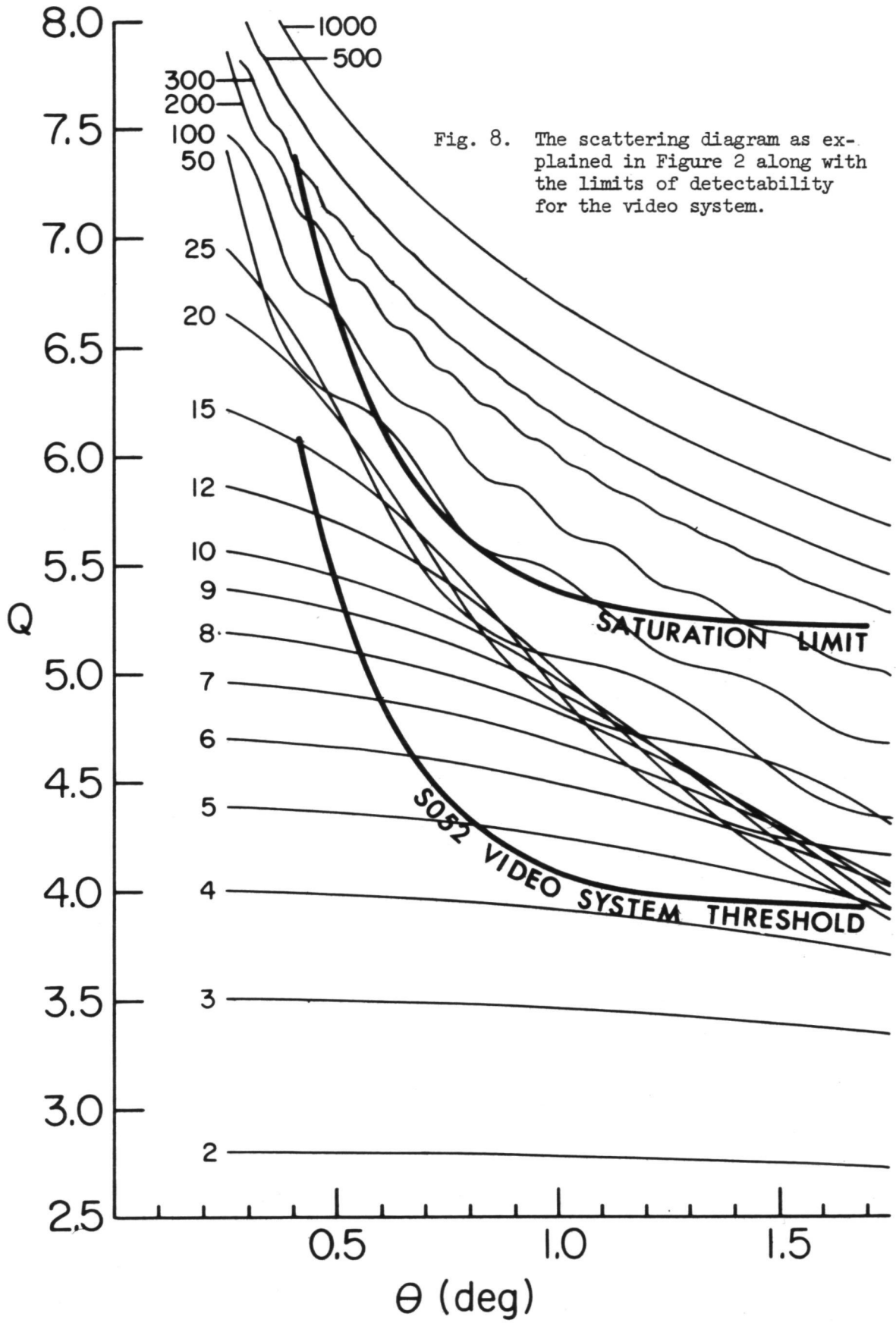

Fig. 8. The scattering diagram as explained in Figure 2 along with the limits of detectability for the video system.

so that

$$(V_t)_{max} \text{ in mm } s^{-1} = 122\ L(m) \quad \text{for } L \quad 75 \text{ m.} \tag{15}$$

The restriction on L here is much smaller that the 200 m used in the photographic method, because the resolution of the video system is less than half that of the film. Saturn's image has a diameter of $.025^{o} \pm 004$. With this resolution limit, distances beyond 75 meters or so from the spacecraft can not be determined accurately (see equation (1)). The space velocities, from equations (2) and (4), also contain L. For L > 75 meters, the velocities so obtained represent only a lower limit. In the presentation of the results, such lower limits will be noted by an asterisk.

The Video Results

A sample of 34 particles was selected for detailed investigation from a six minute portion of tape commencing at 17:34:00 GMT on DOY 220. Figure 9 is a histogram showing the number of particles in the field of view as a function of time. From this total population, 34 particles were selected at the times indicated by the tic marks in the top of the figure. The selection was made so as to include a variety of particle speeds, brightnesses, and sizes. Any bias induced by the selection procedure was unintentional.

At least three sets of measurements were made for each particle so that some measure of uncertainty would be obtained; Table 3 shows the results. The particles are listed chronologically as they appear in Figure 9. Column 2 shows the angular speed of the particle through the field of view. Two values of this quantity could be derived from the positional and time data; the average of these two is shown, along with the standard deviation.

The next two columns are closely related. The one designated by L shows the range of particle distances as inferred by three measurements of particle diameter, a. The entries that are starred probably represent lower limits, since distances beyond 75 m cannot be determined. The radial velocities are found from the L values and the time intervals between their measurements. At least two values for V_r were determined for each particle; their average and standard deviation are shown. Those entries marked by an exclamation point are not internally consistent in that the two values for V_r

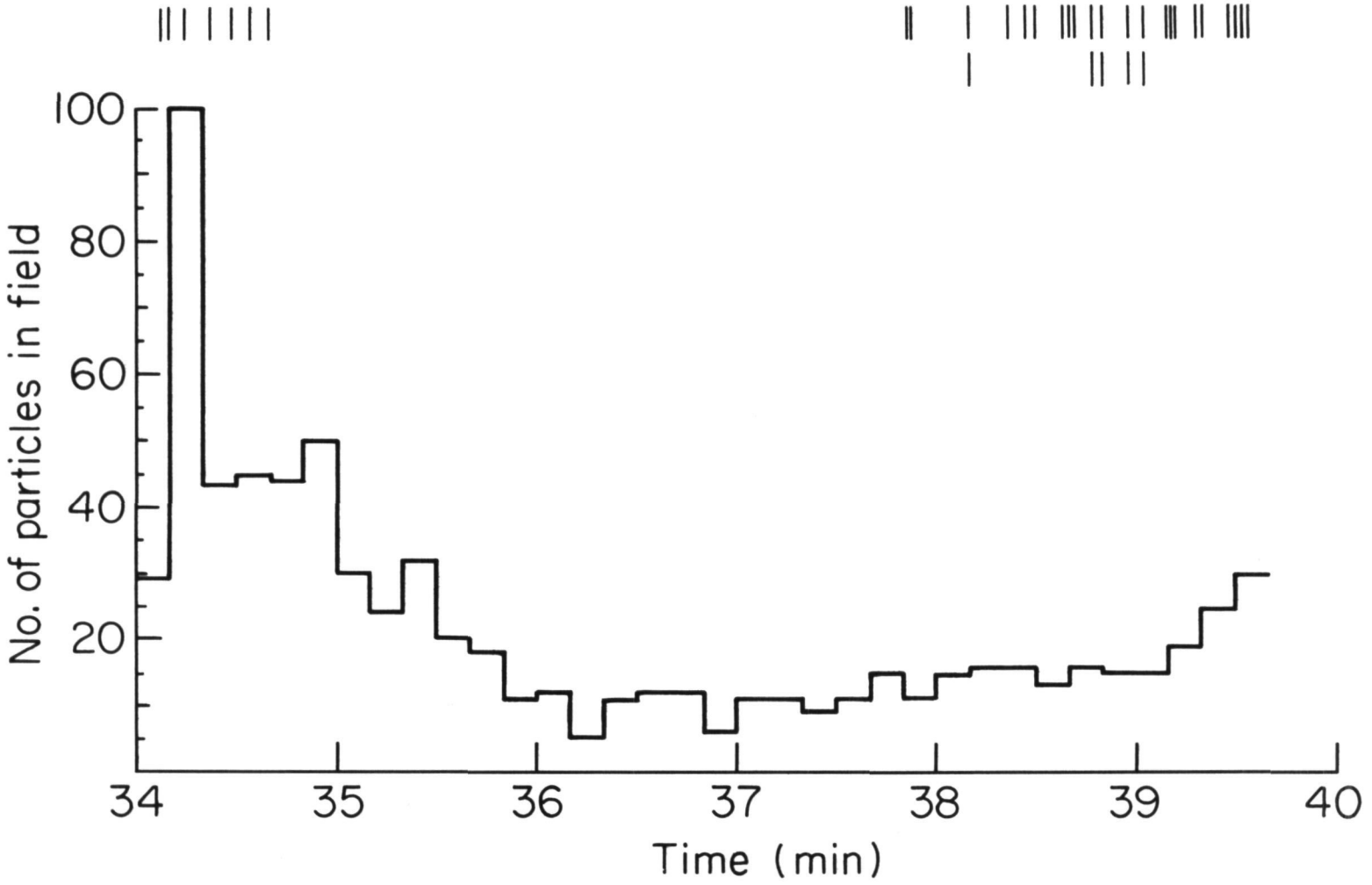

Fig. 9. A histogram showing the number of particles in the field of view as a function of time for a 6 minute portion of video tape starting at 17:34:00 GMT on day 220. The tic marks at the top indicate those particles that were investigated in detail.

Table 3

VIDEO RESULTS

Angular velocity in $deg\text{-}s^{-1}$	V_r Radial velocity in $m\text{-}s^{-1}$	L Distance in m	V_t Transverse velocity in $m\text{-}s^{-1}$	ϕ Track angle in deg	ρ Particle radius in μm lower limit	best estimate	upper limit
1.28 ± .13	15. ± 8.	25-48	0.908 ± .217	93	5	6	7
1.29 ± .42	! 6.7 ± 56.	24-48	0.647 ± .254	184	22	25	95
2.59 ± .65	! 7.0 ± 21.	24-28	1.105 ± .071	177	22	40	250
6.66 ± .82	8.5 ± 0.5	13-15	1.540 ± .017	219	40	50	60
0.34 ± .06	! 2. ± 14.	48-72	0.413 ± .064	229	8	9	10
1.66 ± .13	! 2. ± 14.	10-16	0.333 ± .006	185	40	50	75
0.63 ± .25	0. ± 0.	62-62	0.684 ± .279	277	15	20	25
2.27 ± .47	10. ± 2.	21-29	0.968 ± .400	168	20	30	50
7.10 ± .18	!-29. ± 99.	14-29	0.240 ± .212	348	20	25	40
4.75 ± .86	7. ± 10.	17-22	1.514 ± .150	210	11	15	23
0.42 ± .10	! 11. ± 22.	*70-86	0.494 ± .154	74	5	12	50
0.24 ± .02	! -3. ± 6.	62-72	0.273 ± .048	351	23	30	40
1.25 ± .37	! 24. ± 60.	29-62	0.740 ± .047	96	40	40	40
1.51 ± .31	20. ± 3.	31-48	0.921 ± .110	185	15	25	40
1.58 ± .35	34. ± 30.	31-48	0.708 ± .365	175	20	30	40
0.81 ± .07	! 6. ± 20.	61-72	0.807 ± .139	220	25	45	75
3.50 ± .31	6.9 ± .07	22-24	1.370 ± .001	171	7	8	24
3.32 ± .14	! 36. ± 51.	20-26	0.949 ± .683	186	25	50	150
3.80 ± .25	! 47. ± 147.	25-48	1.731 ± .626	44	10	25	35
3.06 ± .21	4.7 ± 1.	17-19	0.947 ± .003	170	20	30	50
6.00 ± .92	25. ± 11.	18-24	2.078 ± .088	173	5	7	9
2.40 ± .19	! -2. ± 4.	8-9	0.353 ± .018	214	40	50	60
1.22 ± .26	65. ± 127.	*62-108	1.294 ± .762	218	7	8	10
1.08 ± .06	! 24. ± 46.	33-62	0.733 ± .448	259	8	10	12
0.87 ± .00	! 11. ± 15.	*86-108	1.453 ± .191	301	6	8	10
7.05 ± .58	! 22. ± 61.	14-19	1.877 ± .266	175	8	9	10
0.87 ± .06	! 28. ± 8.	*62-108	1.306 ± .434	5	5	7	12
5.30 ± 1.1	! 44. ± 173.	16-34	2.102 ± .283	285	7	25	40
5.47 ± 1.2	! 9. ± 13.	20-23	2.038 ± .311	168	12	25	200
2.05 ± 1.9	! -5. ± 27.	62-72	2.543 ±2.210	246	12	25	150
3.18 ± .25	! 12. ± 40.	24-31	1.349 ± .205	168	9	15	25
5.80 ± .16	31. ± 22.	12-22	1.774 ± .566	171	10	11	12
0.41 ± .18	! 0.6 ± 78.	43-48	0.319 ± .130	274	40	40	40
1.18 ± .83	! 9. ± 13.	62-72	1.352 ± .849	270	15	25	30
Average	14		1.177			24	
Average error	35		0.309				

! Uncertainty is so large that result might not be meaningful for that particle.

* The value is probably a lower limit.

have opposite signs or one value of V_r was zero. An entry so designated might not be meaningful for describing the motion of that single particle. Nevertheless, the results are included because of their importance in a statistical sense.

The average transverse velocities along with the standard deviations are shown in the fifth column. These also depend on the L measurements (see equations (2) and (4)), and those entries that are starred may be lower limits. The direction of particle motion, corrected for the unequal scale factor, is shown in the next column. Consider a right-handed coordinate system superimposed over the TV monitor screen with positive x to the right side as viewed. A ϕ of 0° is along the x axis in the positive direction, and ϕ of 90° is "up" on the screen. The uncertainty in this measurement is small--less than a few degrees.

The last three columns represent best estimates and uncertainties in particle radius. For each particle, at least three points were placed on the scattering diagram and a "best estimate" was made. Large and small limits were also established. It is interesting to note that the average value of the best estimate column is 24μm. This compares with the value of 27μm found from the photographic method. There is no compelling reason to expect,a priori, that these two size distributions should be similar, but the fact that they do coincide gives one a certain amount of confidence in the correctness of the two methods. This is particularly true since the photometric calibration is entirely different for the two techniques. We also

find for the video data, as with the photographic, that the decrease in particle number with increasing particle size is a real feature of the distribution. The upper cut-off at about 50μm is assumed truly representative of the contamination studied. Larger particles, if they existed, would tend to saturate the video response, and saturation was never quite achieved.

Comparison of Methods

Essentially the same parameters concerning particle contamination can be obtained from either the photographic or video technique. In terms of accuracy, the photographic method is characterized by an error in V_t of the order of 80 mm s^{-1} as opposed to 300 mm s^{-1} for the video. Similarly, the photographic error in V_r is only 9 m s^{-1} compared with 35 m s^{-1} for the video. Also, the photographic method, because of its higher resolution, can be used to fully investigate particles out to 200 meters - more than twice the distance that can be investigated with the video method. And finally, the photographic method may be seen from Tables 1 and 3 to be somewhat more accurate for estimating particle size.

On the other hand, only the video method can handle transverse space velocities larger than a few hundred mm s^{-1}. In this method, almost all of the observed particles can be analyzed, and thus selection effects are far less severe than for the photographic method where only the low velocity tail of the distribution can be studied. The other great advantage of the video method is the ease of data taking. The raw data can be read from a monitor grid and oscilliscope with very little effort compared to the time consuming techniques of densitometer tracing and film position measuring. For these two major reasons, the video method is highly recommended as the best one to use for analyzing the large populations of individual particles necessary to statistically characterize the contamination about Skylab.

References

Henize, K. G. and J. L. Weinberg, Astronomy Through the Skylab Scientific Airlocks, Sky and Telescope, 45, 272-276, 1973.

MacQueen, R. M., J. T. Gosling, E. Hildner, R. H. Munro, A. I. Poland, and C. L. Ross, Proceedings of the Society of Photo-Optical Instrumentation Engineers, 44, 207, 1974.

Poland, A. I., J. T. Gosling, R. M. MacQueen, and R. H. Munro, The Radiance Calibration of the High Altitude Observatory White Light Coronagraph on Skylab, submitted to Applied Optics, 1976.

Van de Hulst, H. C., Light Scattering by Small Particles, John Wiley and Sons, Inc., New York, pp. 103-110, 1957.

II. Analysis of Selected Photometer Data on Contamination, Experiment S073

Introduction

When experiment S073 was initially proposed by Prof. E. Ney of the University of Minnesota in June 1967, it had two objectives: 1. measurement of the surface brightness and polarization of the night sky light over as large a portion of the celestial sphere as possible at several wavelengths in the visible spectrum, and 2. performance of the same experiment with sunlight on the spacecraft to determine the extent and nature of the spacecraft corona. Although the Minnesota hardware concept, a hand-held Gegenschein-zodiacal light-airglow photometer ("GZAP gun"), bears no resemblance to the actual instrumentation flown on Skylab, the dual objectives were maintained; this resulted in a sharing of hardware and operations with Skylab experiment T027 and some duplication in the analysis of the data. In this report we present results on four programs performed during mission SL-2 that were designed to provide data on the spacecraft corona. These programs are outlined in Table 1.

Analysis of SL-2 Contamination Programs

The first contamination program (6-1) was performed on SL-2 mission day 19 with the photometer fixed in position at approximately 95 degrees from the sun. Observations were made in all 10 colors*, from 4000A to 8200A, starting with the spacecraft in the earth's shadow and ending in daylight. The reverse sequence (6-2) was performed later in the same orbit; i.e., daylight to shadow. This program was designed to provide information in near real time on the level of scattered light by particulate material around Skylab; our quick-look analysis at JSC indicated that

*4000, 4760, 5080, 5300, 5577, 6080, 6300, 6435, 7100, 8200Å.

Table 1

Selected SL-2 observing programs containing photometric data on the optical environment of Skylab

Run number	Mode	Photometer Extension (distance from spacecraft)	Program description
6-1	1a	5.5m	Fixed in position at 95 degrees from the sun as vehicle moved from night to day; 9 cycles of 10 colors: 7.5 night, 1.5 day.
6-2	1a	1m	Fixed in position at 95 degrees from the sun as vehicle moved from day to night; 9 cycles of 10 colors: 2.5 day, 6.5 night.
12	3d	1m	Scan in azimuth at fixed elevation, during satellite day. 10 colors per orbit, 8 orbits.
13	3d	5.5m	Scan in azimuth at fixed elevation, during satellite day. 10 colors per orbit, 8 orbits.

the spacecraft corona was minimal. A more detailed, but still preliminary, analysis of these data (Weinberg, et al., 1974) indicated that there were levels of sky brightness in daylight only 5% above those at night; i.e., low light level astronomical observations were able to be made from outside the earth's shadow. Subsequent fixed-position and sky scanning programs measured higher levels of daytime sky radiance, but analysis of those programs could not be completed until additional data were obtained on program timing and on illumination conditions of the vehicle and photometer/camera system.

In an independent study of the data from these programs (Table 1), Muscari and Jambor (1975) conclude that factor-of-100 brightness changes observed in runs 6-2 and 12 are a result of sunlight scattered by a contaminant cloud around Skylab. We have evaluated these data in detail; we find that the observed changes in brightness are a direct result of stray light from illuminated parts of the vehicle outside the photometer field of view. We find no evidence for a spacecraft corona to the photometer's limit of detection of a change in background (see section III of this report). In the following we examine each of these runs (Table 1) in detail.

A. Run 6-2

As noted earlier, the photometer was fixed in position at 95 degrees from the sun (toward the north galactic pole) as the vehicle moved from day to night. The measurements are tabulated as a function of color, GMT time, and time from sunrise/sunset in Appendix 1. The occasional groupings of high dark current indicate times when the spacecraft was near the South Atlantic anomaly.

In Figure 1 we have plotted day sky brightness normalized to the night value as a function of time for four of the 10 observed wavelengths. It is unfortunate that the program was started at the wrong time; thus, there are only a few data points in daylight. Examination of all the data indicates that the sky signal was decreasing as early as five minutes before sunset. The nature of this time decay, its rate of change and its position, is of particular interest.

Since data concerning the characteristics of sunrise/sunset were not readily available, we determined the apparent altitude versus time of

Figure 1. Day sky brightnesses normalized to the nightsky level; run 6-2.

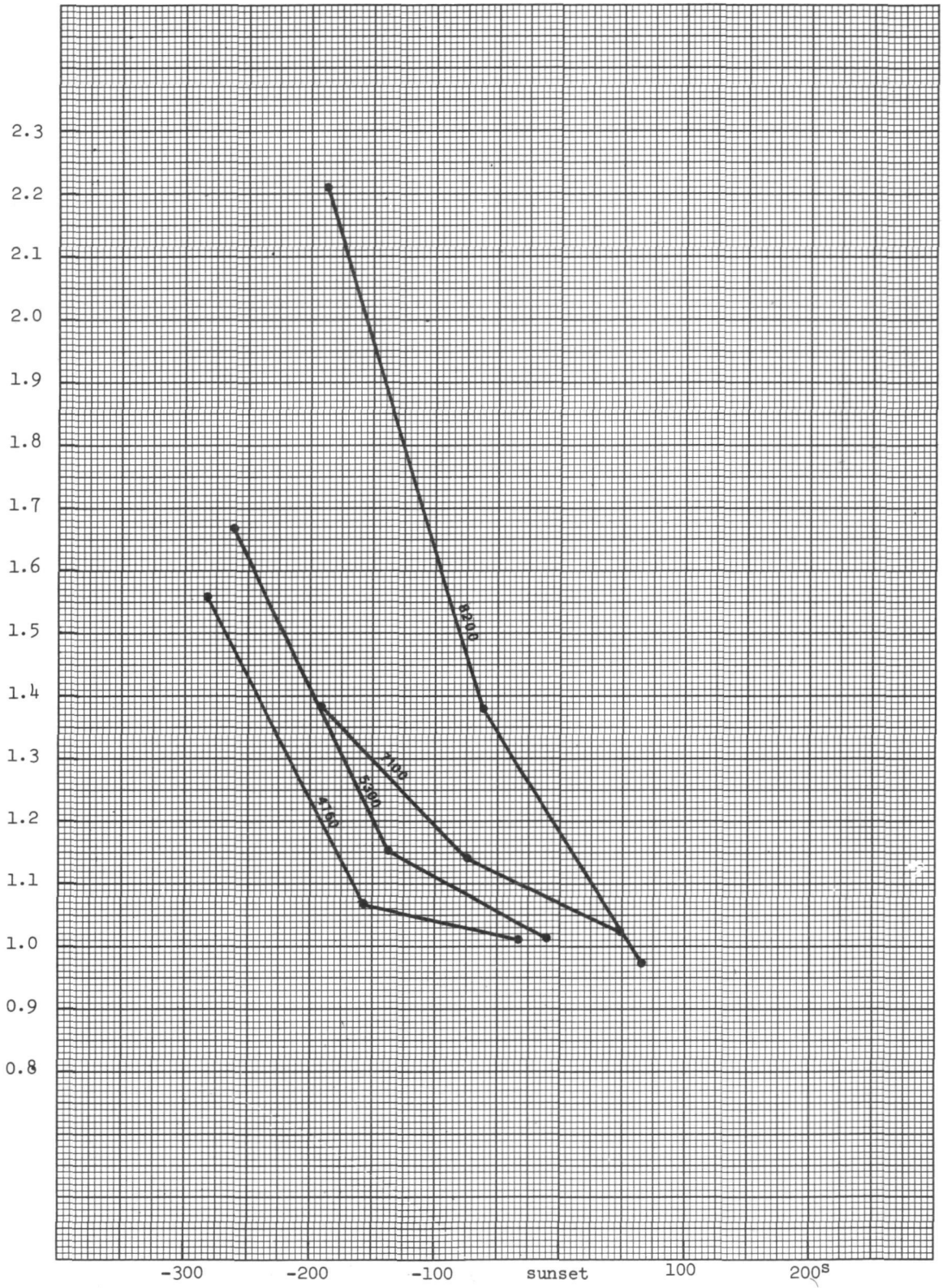

sunrise/sunset as a function of beta angle (see Appendix 2). For each altitude, we calculated the number of air masses traversed by the sun's rays and, using the atmospheric transmission given by Allen (1973), the color and time characteristics of apparent sunrise/sunset. The results are shown in Figure 2. No attempt was made to model the day/night 5577 and 6300 airglow characteristics. These data, as expected, have a different time rate of change than the data at continuum wavelengths. Note that the decay rates shown in Figure 2 begin only 20 seconds before geometrical sunset and continue for more than 50 seconds after geometrical sunset. A comparison with the observations shown in Figure 1 indicates that sunrise/sunset is not responsible for the observed rate of change of sky brightness.

The next step in the analysis involves a determination of the irradiance due to the sunlit earth. The time period from terminator set (line of demarcation of sunlit earth directly below spacecraft) to sunset was chosen for this modeling. Since the irradiance is proportional to both the area of the sunlit earth seen by the spacecraft and the absorption of the atmosphere as the sun's rays penetrate and are reflected back to the spacecraft, the modeling must include both effects. The reflection characteristic of the earth was assumed to be wavelength independent; thus, the irradiance at the spacecraft is

$$I(T) \propto A(T) e^{-\tau_\lambda m(T)},$$

where $A(T)$ is the relative projected area of the illuminated earth as a function of the solar depression angle T, τ_λ is the absorption per unit air mass at wavelength λ, and $m(T)$ is the number of air masses traversed as a function of T (see Appendix 3). The solar depression angle can be

Figure 2. Color/time dependence of apparent sunrise/sunset.

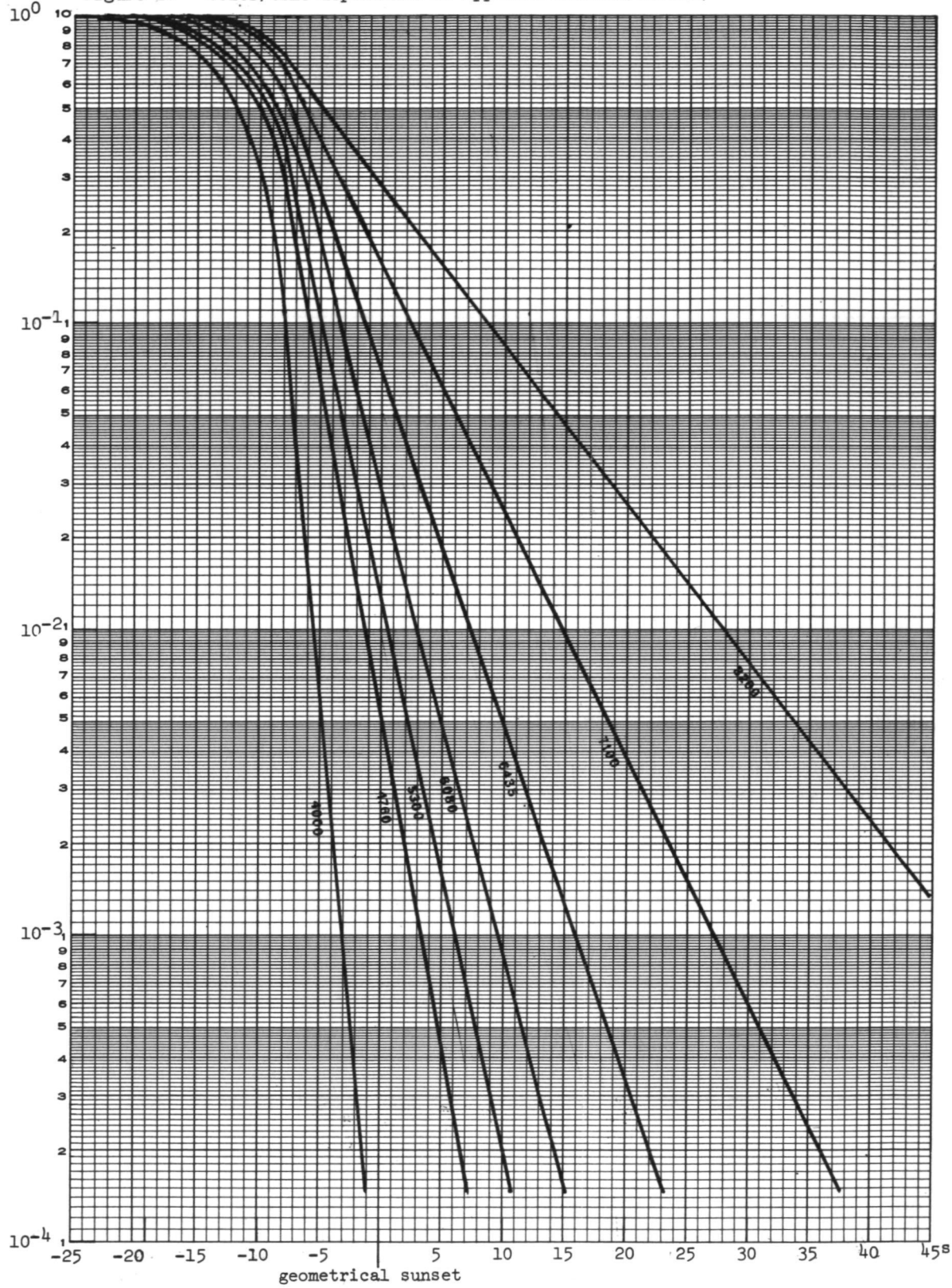

related to time through the orbital angular velocity and beta angle, and thus the relative irradiance can be determined as a function of time. The result is plotted in Figure 3 for the beta angle during Run 6-2. As in the case of direct sunrise modeling, the effect on the airglow lines was not considered.

As in Figure 2, there is a strong wavelength dependence in the time decay characteristic. Note that a significant rate of decay is occurring as early as 300 seconds before sunset and that the blue end of the spectrum is diminished before the red end by as much as 50 to 100 seconds before sunset. The similarity of these time characteristics to the observed decay rates (Figure 1) suggests strongly that the sunlit earth is the primary source of the observed changes.

We also investigated the possibility that the change in signal was caused by direct (on-axis) earthlite. The earth was "behind" the photometer, i.e. more than 90° from the line of sight at all times. Conclusive evidence for the source being "off-axis" is shown in Figure 4, which is a copy of a photograph taken during the "high signal" period with the 16 mm Data Acquisition Camera (DAC) that was boresighted with the photometer. Note that the sky region defined by the camera sunshield was exposed correctly; i.e., the sky is dark, and stars are as clearly visible as they are at night. Note, also, that the inner portions of the sunshield are overexposed; this can only be caused by the sunshield's knife edges being illuminated by a source outside the field of view (the camera and photometer fields of view are 15 and 6 degrees, respectively). A study of the geometry indicates that the spacecraft discone antenna was approximately opposite the bright corner and was therefore responsible for some and perhaps all of the off-axis brightness seen by the camera and the

Figure 3. Color/time dependence of the irradiance of the sunlit earth.

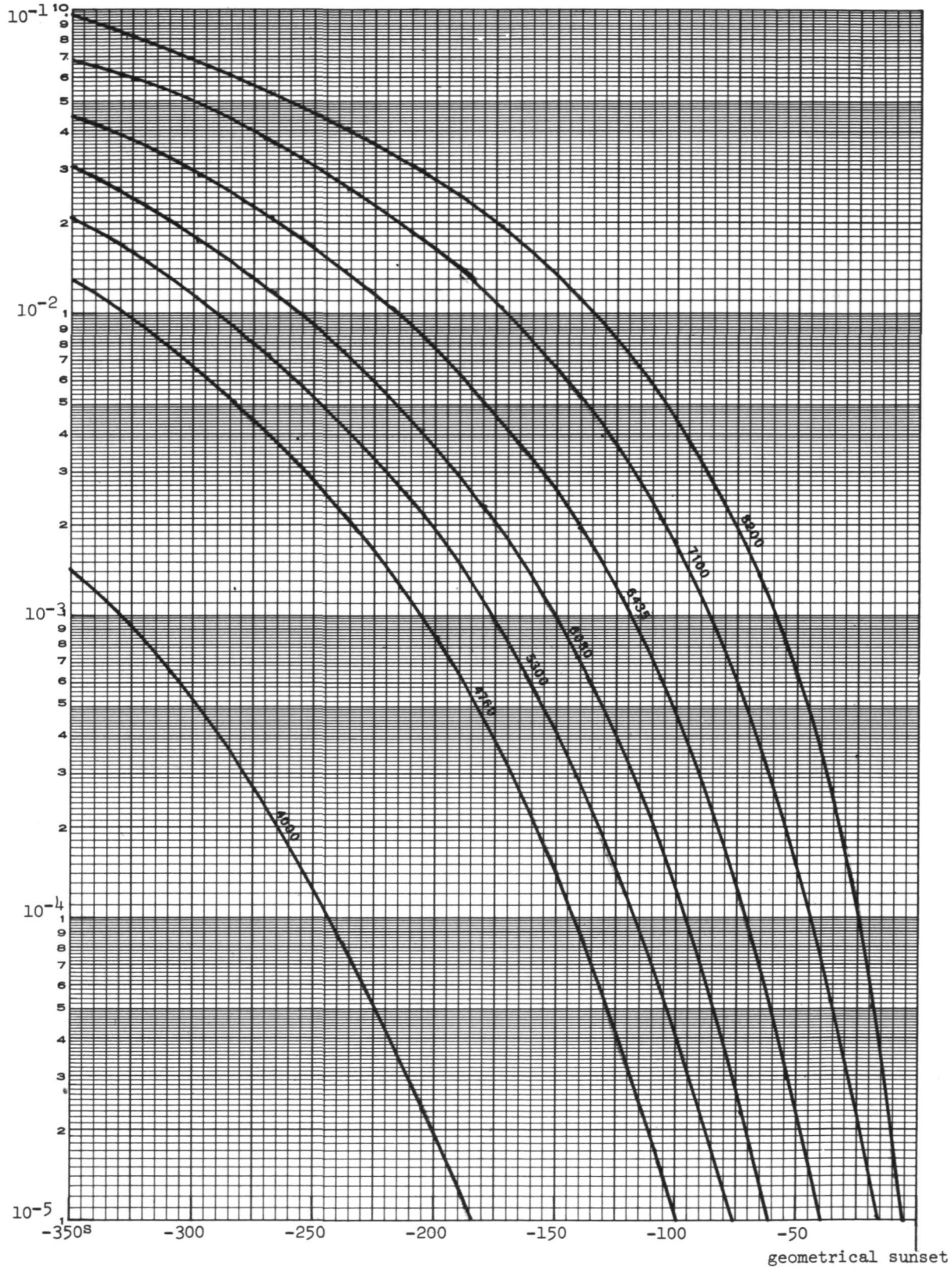

photometer.

Various parts of the illuminated (by the sunlit earth) spacecraft were found to be within 90° of the line of sight, with the discone antenna being approximately 50° from the line of sight. The short, low-rejection sunshield was used for these observations, and this sunshield does not have adequate rejection for bright sources this close to the line of sight.

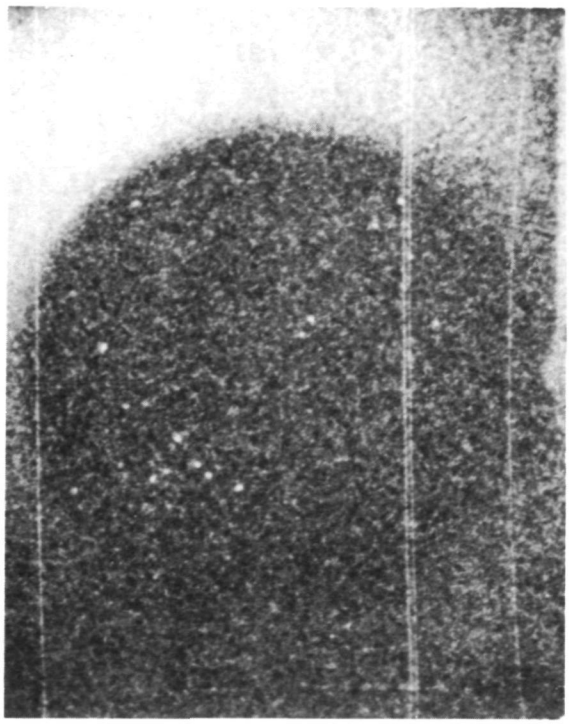

Figure 4. One of a series of DAC photographs taken during run 6-2. Note the dark sky at the center and the illuminated portion of the sunshield in the upper left.

B. Run 6-1

Muscari and Jambor (1975) reported that there was no night/day change in signal for this observation; this is expected, because the last data group was taken only 60 seconds after sunrise. Curves similar to Figures

2 and 3 for sunrise show that significant earthlight was not present until more than 100 seconds after sunrise. Full direct sunlight was present within 20 seconds after sunrise.

C. Run 12

The analysis of these data are more complex, because the photometer was scanning in azimuth (i.e., in a plane approximately perpendicular to the direction to the sun) during the measurement cycle. In this program the photometer observed over a range of azimuth at fixed elevation; the scan was made in a particular color, the photometer retraced its scan at the next color, etc., until all 10 colors were used. The photometer then waited until it reached the same starting place in the next orbit and it repeated the cycle. Multicolor scans of a 60^{o} region of azimuth were obtained in this program on successive orbits, some scans with the photometer 1 m from the spacecraft and some (run 13) at 5.5 m from the spacecraft.

As noted by Muscari and Jambor (1975), each scan was started (and completed) during spacecraft day. The program was initiated only 11 seconds after sunrise, however; in orbit 1 it stopped at sunrise plus 110 seconds and in orbits 2 and 3 it stopped at sunrise plus 182 seconds. This difference was due to an anomaly in the instrument preparation routine; in the first orbit only the last 5 filters were used. This difference is important since the 8200A data in orbit 1 were taken starting only 80 seconds after sunrise; in orbits 2 and 3 these data were taken starting 150 seconds after sunrise. This is the filter that showed the largest rise in signal, and these are the data that Muscari and Jambor use to determine the level of "contamination".

Figure 5 is a computer-generated plot of output signal versus time

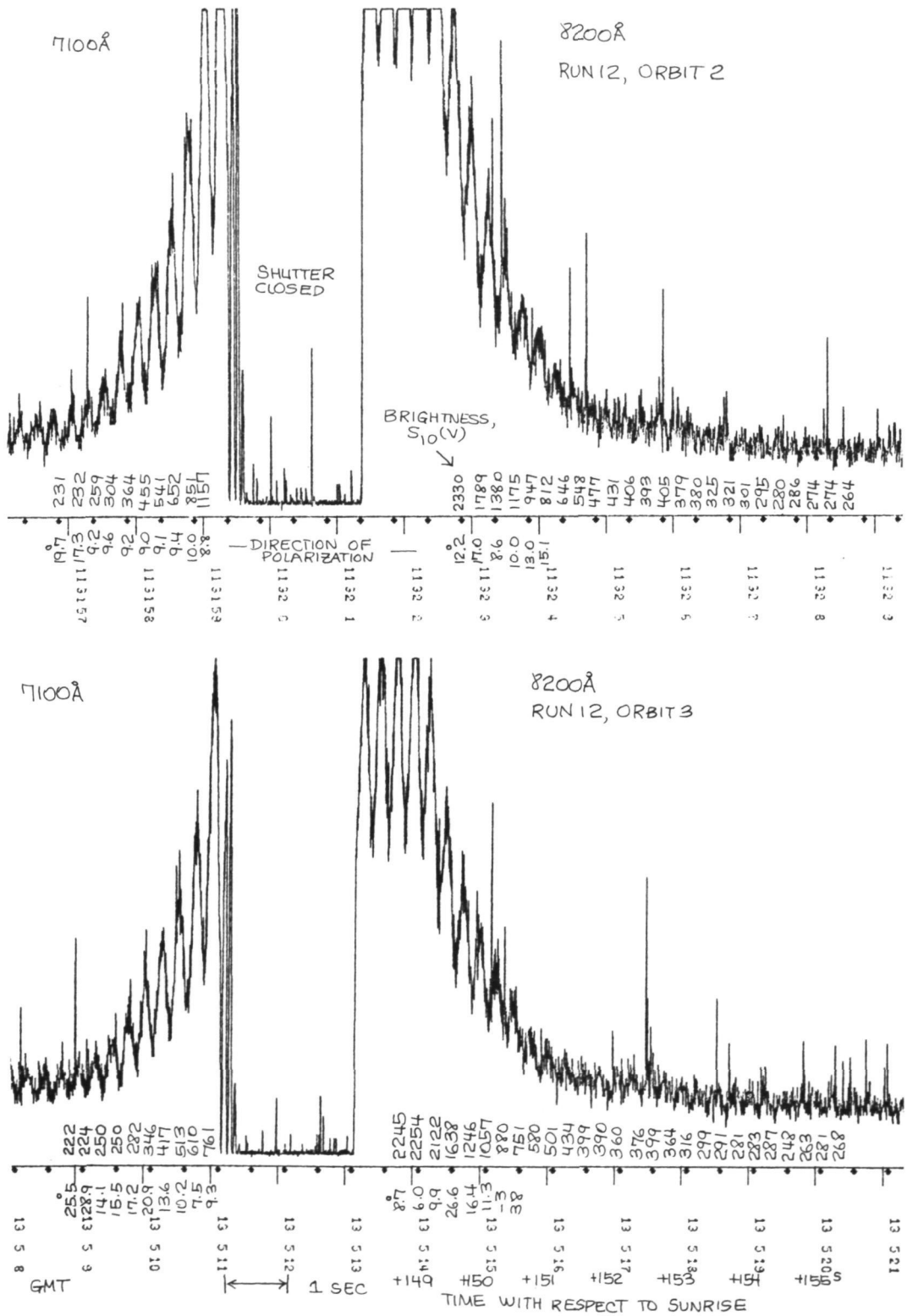
7100Å
8200Å
RUN 12, ORBIT 2
SHUTTER CLOSED
BRIGHTNESS, S_{10}(V)
DIRECTION OF POLARIZATION
7100Å
8200Å
RUN 12, ORBIT 3
GMT
1 SEC
TIME WITH RESPECT TO SUNRISE

FIGURE 5

for orbits 2 and 3. The signal shown at the left of each plot is the output at 7100A with the azimuth moving towards its upper limit. At the upper limit the shutter closed (dark current level is shown left of center), the 8200A filter moved into position, the shutter opened, and the azimuth (after a 1 sec delay) moved toward its lower limit. The scanning rate was 3.87°/sec. The sinusoidal variation of output at the higher levels is due to the modulation of the polarized component by the rotating polaroid; the large amplitude indicates that the signal was highly polarized. Brightnesses marked along the baseline correspond to data averaged over $\frac{1}{4}$-second intervals ending at the position of the value; also indicated are the relative phase angles of the polarized component. The limiting effect of the telemetry system (5 volts) is clearly visible on the high signal levels in Figure 5. The difference in levels of the maximum signal between the two orbits is probably due to the fact that the azimuth control was accurate only to $\pm$ 1.4 degrees. At the large rate of increase of signal, even a small difference in azimuth could produce the difference in signal level between the two orbits. Muscari and Jambor claim that this difference is due to the gradual dissipation of the contaminant cloud between orbits 2 and 3.

Characteristics similar to Figures 2 and 3 were derived for the beta angle during run 12. They show that the earthlight at 8200A increases by a factor of 3 between 80 and 140 seconds after sunrise; thus, the signals at any particular point in the scan should differ by that amount between orbits 1 and 2. Muscari and Jambor's data show a difference of a factor of 2.5 at azimuth 185° between orbits 1 and 2. The fact that the signal increase was a strong function of azimuth also suggests that the source is light reflected off the spacecraft. Difficulties

in the telemetry system require that the raw azimuth data be corrected. When these corrections are made, the signal increases as a function of azimuth for orbits 2 and 3 are almost identical, not significantly different as indicated by Muscari and Jambor. Other differences noted by Muscari and Jambor, especially the spectral differences, can also be shown to be similar to the earthlight color/time characteristics.

The difference in direction of polarization of the enhanced signal (Figure 5) is still further evidence against contamination as the source of the enhancement. The direction of polarization for the zodiacal light or for scattering by particulates near the spacecraft is the same - perpendicular to the direction to the sun. Only multiply-scattered light (e.g., light scattered off the vehicle and seen by the sunshield baffles) can give a different direction of polarization.

In summary, there is firm evidence for stray light from the sunlit earth in the SL-2 photometer observations analyzed by Muscari and Jambor (1975); we find no evidence for a detectable spacecraft corona in these observations. In the subsequent section we show further that the photometer would not detect the column brightness from the typical level of particulates observed by the S052 coronagraph.

References

C. W. Allen, Astrophysical Quantities, 3rd edition, the Athlone Press, 1973.

J. A. Muscari and B. Jambor, Final Report, Skylab Experiment T027, ED-2002-1776, Martin-Marietta, June 1975.

J. L. Weinberg, R. D. Mercer, and R. C. Hahn, The optical environment of Skylab, Mission SL-2, Bull. AAS, 6, 337, 1974.

III. The Composite Picture

Photographs obtained with the S052 coronagraph and photoelectric data obtained with the photometer of experiments S073 and T027 contain unique data on the Skylab spacecraft corona. Particle tracks on the S052 photographs have provided data on discrete contaminant particulates at small scattering angles: number, size, distance, velocity. Further analysis of selected photometric data from Mission SL-2 showed no evidence for integrated light from contaminant particulates down to our threshold of detection of a few $S_{10}(V)^*$. It is of interest to determine the approximate sensitivity of the photometer to the brightness contributed by individual particles and to compare the photographic (small angle) and photoelectric (large angle) results.

We make the following assumptions:

1. The average particle size ρ is 25 microns in radius;
2. The particles are uniformly distributed out to a distance L of 200 meters from the spacecraft;
3. The energy scattered from each particle at scattering angles of $90^\circ \pm 10^\circ$ is .05 of the energy of an isotropic scatterer whose scattering cross section is assumed to be equivalent to its geometrical cross section.

The scattered energy E_s at the photometer objective lens is

$$.05 \int_0^L I_\odot \, \pi \rho^2 \, \frac{1}{4\pi} \, \frac{\pi r^2}{L^2} \, \sigma \, dv,$$

where σ is the number density of particles, ρ is the particle radius, and $I_\odot$ is the solar flux per unit area.

---

* Equivalent number of 10th magnitude solar (G2V) stars per square degree at mean solar distance. At 5300A, 1 $S_{10}(V)$ = 1.30 x 10^{-9} ergs/cm^2 sec sterad Å = 4.5 x 10^{-16} $B_\odot$.

Figure 1.

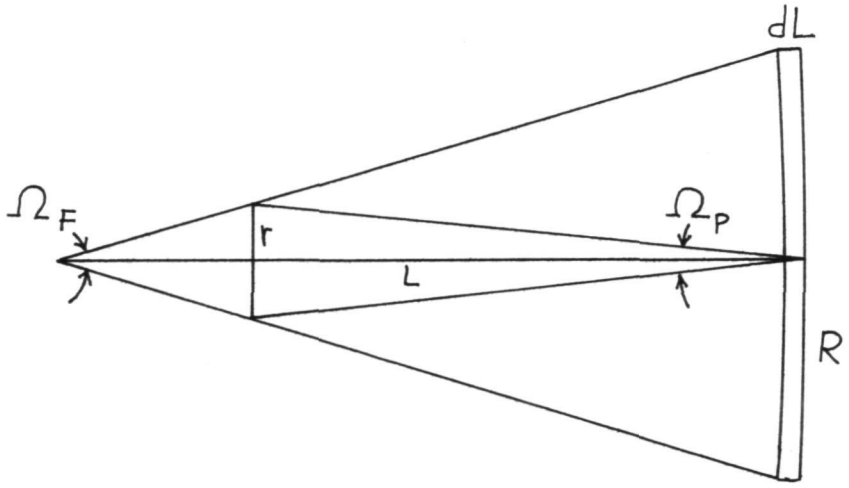

r radius of photometer objective lens
Ω_F solid angle of the photometer field of view
Ω_P solid angle subtended by the objective at distance L
R radius of photometer area of view at L
A photometer area of view at L

$dV = A\ dl = L^2\ dl$

Referring to Figure 1, this reduces to

$$E_S = .05 \int_0^L I_\odot \frac{\rho^2}{4} \pi r^2 \sigma \Omega_F \ dl$$

or

$$E_S = .05\ I_\odot \frac{\pi \rho^2 r^2}{4} \sigma \Omega_F\ L.$$

The energy at the photometer due to the direct solar radiation is

$$B_\odot \pi r^2 \Omega_F$$

or

$$\frac{I_\odot}{\Omega_\odot} \pi r^2 \Omega_F .$$

Normalizing the radiation from the particles to the direct solar radiation gives

$$\frac{.05\, I_\odot \; \frac{\pi \rho^2 \; r^2}{4} \sigma \; \Omega_F \; L}{\frac{I_\odot}{\Omega_\odot} \; \pi r^2 \; \Omega_F}$$

$$= \frac{.05 \; \rho^2 \sigma \; L \; \Omega_\odot}{4} .$$

Using the values assumed earlier for ρ and L and the solid angle $\Omega_\odot$ of the sun, we obtain $1.06 \times 10^{-7} \sigma$.

The photometer output is calibrated in $S_{10}(V)$ units (see earlier). After subtracting the brightness contribution of resolved stars, the total sky brightness for the region in question is approximately 100 $S_{10}(V)$. Total instrument reproducibility and the method of differencing day-night or night-day sky brightness combine to give a minimum detectable brightness change of from 1 to 3 $S_{10}(V)$. Using the value of 3 $S_{10}(V)$, we obtain a minimum detectable number density of particulates of

$$= \frac{3 \; S_{10}(V) \times 4.5 \times 10^{-16} \; B_\odot / S_{10}(V)}{1.06 \times 10^{-7}}$$

$$= 1.27 \times 10^{-8} \text{ particles/cm}^3 .$$

The number of particles per S052 field (see Figure 9 of section I) ranged from 5 to 100. For the typical number of 10 particulates in the S052 volume of view out to 200 m, the number density is 2×10^{-9} cm^{-3}.

Our inability to distinguish a day-night or night-day change in brightness which could be attributed to contamination is therefore consistent with the S052 analysis which finds the typical number density to be below our column brightness threshold for detection. However, there were periods of a factor-of-ten higher concentration that would bring the particulate background up to the level of detectability of the photometer. Since this increased level of particulates had no preferred direction, we do not associate these levels with dumps or thruster firings.

APPENDIX 1

Run 6-1

GMT day	hr:min:sec	time with respect to sunrise (sec)	color, nominal	total signal (volts)	dark current (volts)	net signal (volts)	net signal (S_{10}(V))
163	20:14:27.9		4000 Å	>10			
	:39.9		4760	>10			
	:51.9		5080	>10			
	15:03.9		5300	>10			
	15:15.9		5577	1.32	.10	1.22	13788
	:29.9		6080	1.02	.1	1.01	3222
	:41.9		6300	.43	.1	.33	5763
	:53.9		6435	.68	.11	.57	1721
	16:05.9		7100	.48	.11	.37	1235
	:17.9		8200	.63	.10	.53	2876
	:31.9		4000	.19	.10	.09	595
	:44.0		4760	.40	.10	.30	690
	:56.0		5080	.23	.11	.12	302
	17:08.0		5300		gain change		
	:20.0		5577	.42	.11	.31	350
	:34.0		6080	1.05	.11	.94	300
	:46.0		6300	.33	.12	.21	367
	:58.0		6435	1.07	.12	.95	287
	18:10.0		7100	1.03	.11	.92	307
	:22.0		8200	.80	.11	.69	374
	:35.9		4000	.52	.11	.41	271
	:47.9		4760	1.10	.12	.98	256
	:59.9		5080	1.12	.12	1.00	252
	19:11.9		5300	1.18	.11	1.07	256
	:23.9		5577	.36	.11	.25	282
	:38.9		6080	.90	.11	.79	252
	:49.9		6300	.31	.11	.20	349
	20:01.9		6435	.96	.11	.85	256
	20:13.9		7100	.92	.11	.81	270
	:25.9		8200	.65	.11	.54	293
	:40.0		4000	.51	.11	.40	264
	:52.0		4760	1.05	.11	.94	216
	21:04.0		5080	1.09	.11	.98	247
	:16.0		5300	1.11	.11	1.00	239
	:28.0		5577	.35	.11	.24	271
	:42.1		6080	.88	.11	.77	246
	:54.0		6300	.31	.11	.20	349
	22:06.0		6435	.85	.11	.84	254
	:18.0		7100	.91	.11	.80	267
	:30.0		8200	.65	.11	.54	293
	:44.1		4000	.51	.11	.40	264
	:56.1		4760	1.06	.11	.95	218
	23:08.1		5080	1.08	.11	.97	245
	:20.1		5300	1.14	.11	1.03	246
	:32.1		5577	.34	.11	.23	260

Run 6-1, continued

GMT day	hr:min:sec	time with respect to sunrise (sec)	color, nominal	total signal (volts)	dark current (volts)	net signal (volts)	net signal (S_{10}(V))
163	20:23:46.1		6080 Å	.88	.11	.77	246
	:58.1		6300	.30	.11	.19	332
	24:10.1		6435	.94	.11	.83	251
	:22.1		7100	.91	.11	..80	267
	:34.1		8200	.63	.10	.53	288
	:48.1		4000	.50	.11	.39	258
	25:00.2		4760	1.05	.11	.94	216
	:12.2		5080	1.10	.11	.99	250
	:24.2		5300	1.13	.11	1.02	244
	:36.2		5577	.34	.11	.23	260
	:50.2		6080	.88	.11	.77	246
	26:02.2		6300	.30	.11	.19	332
	:14.2		6435	.94	.11	.83	251
	:26.2		7100	.91	.11	.80	267
	:38.2		8200	.63	.10	.53	288
	:52.2		4000	.50	.11	.39	258
	27:04.2		4760	1.05	.11	.94	216
	:16.2		5080	1.09	.11	.98	247
	:28.2		5300	1.13	.11	1.02	244
	:40.2		5577	.34	.12	.22	249
	:54.3		6080	.88	.11	.77	246
	28:06.2		6300	.28	.11	.17	297
	:18.2	- 110	6435	.93	.11	.82	247
	:30.2	- 99	7100	.90	.11	.79	264
	:42.2	- 86	8200	.64	.11	.53	288
	:56.3	- 72	4000	.50	.11	.39	258
	29:08.3	- 60	4760	1.05	.11	.94	216
	:20.3	- 48	5080	1.09	.11	.98	247
	:32.3	- 36	5300	1.13	.11	1.02	244
	:44.3	- 22	5577	.34	.12	.22	249
	:58.3	- 10	6080	.88	.11	.77	246
	30:10.3	+ 2	6300	.29	.11	.18	314
	:22.3	+ 14	6435	.96	.11	.85	257
	:34.3	+ 26	7100	.94	.11	.83	277
	:46.3	+ 38	8200	.78	.11	.67	363
	31:00.4	+ 52	4000	.51	.12	.39	258
	:12.4	+ 64	4760	1.07	.12	.95	218
	:24.4	+ 76	5080	1.16	.11	1.05	264
	:36.4	+ 88	5300	1.29	.12	1.07	256
	:48.4	+ 100	5577	.42	.12	.30	339
	32:02.4	+ 114	6080	.90	.11	.79	252
	:14.4	+ 126	6300	.32	.12	.20	349
	:26.3	+ 138	6435	.96	.11	.86	260
	:38.3	+ 150	7100	.93	.11	.82	274
	:50.3	+ 162	8200	.85	.11	.74	401

Run 6-2

GMT day	hr:min:sec	time with respect to sunset (sec)	color, nominal	total signal (volts)	dark current (volts)	net signal (volts)	net signal (S_{10}(V))
163	21:24:23.0	- 296	4000 Å	.58	.11	.47	310
	:35.0	- 284	4760	1.02	.11	.91	209
	:47.0	- 272	5080	1.25	.11	1.14	288
	:59.0	- 260	5300	1.16	.11	1.05	250
	25:11.0	- 248	5577	.41	.11	.30	338
	:25.0	- 234	6080	.66	.10	.56	180
	:37.0	- 222	6300	.33	.11	.22	390
	:49.0	- 210	6435	.73	.11	.62	188
	26:01.0	- 198	7100	.78	.11	.67	223
	:13.0	- 186	8200	.84	.11	.73	398
	:27.1	- 172	4000	.39	.11	.28	184
	:39.1	- 160	4760	.75	.12	.63	144
	:51.1	- 148	5080	.79	.10	.69	174
	27:03.1	- 136	5300	.82	.10	.72	172
	:15.1	- 124	5577	.30	.12	.18	203
	:29.1	- 110	6080	.62	.12	.50	161
	:41.1	- 98	6300	.27	.12	.15	261
	:53.1	- 86	6435	.67	.13	.54	163
	28:05.1	- 74	7100	.68	.13	.55	182
	:17.1	- 62	8200	.60	.14	.46	249
	:31.2	- 48	4000	.46	.20	.26	175
	:43.2	- 36	4760	.83	.22	.61	141
	:55.2	- 24	5080	.85	.25	.60	151
	29:07.2	- 12	5300	.93	.30	.63	151
	:19.2	0	5577	.44	.34	.10	119
	:33.2	+ 14	6080	.83	.39	.44	142
	:45.2	+ 26	6300	.55	.45	.10	176
	:57.2	+ 38	6435	.99	.50	.49	147
	30:09.2	+ 50	7100	1.04	.55	.49	163
	:21.2	+ 62	8200	.94	.61	.33	177
	:35.2	+ 76	4000	.96	.66	.30	198
	:47.2	+ 88	4760	1.34	.74	.60	139
	:59.2	+ 100	5080	1.46	.79	.67	168
	31:11.2	+ 112	5300	1.54	.83	.71	169
	:23.2	+ 124	5577		data outage		
	:37.2	+ 138	6080	1.51	1.01	.50	160
	:49.2	+ 150	6300	1.16	1.06	.10	176
	32:01.2	+ 162	6435	1.65	1.12	.53	159
	:13.2		7100	1.71	1.19	.52	175
	:25.2		8200	1.01	1.25	.36	198
	:39.3		4000	1.63	1.30	.33	220
	:51.3		4760	1.95	1.35	.60	139
	33:03.3		5080	2.01	1.40	.61	155
	:15.3		5300	2.13	1.44	.69	164
	:27.3		5577	1.68	1.47	.21	233

Run 6-2, continued

GMT day	hr:min:sec	time with respect to sunset (sec)	color, nominal	total signal (volts)	dark current (volts)	net signal (volts)	net signal (S_{10}(V))
163	21:33:41.3		6080 Å	2.04	1.50	.54	172
	:53.3		6300	1.76	1.52	.24	414
	34:05.3		6435	2.08	1.54	.54	163
	:17.3		7100	2.06	1.54	.52	174
	:29.3		8200	1.90	1.54	.36	196
	:43.3		4000	1.88	1.53	.35	234
	:55.3		4760	2.07	1.51	.56	129
	35:07.3		5080	2.14	1.49	.65	165
	:19.3		5300	2.14	1.44	.70	168
	:33.9		5577	1.58	1.40	.18	209
	:45.3		6080	1.91	1.35	.56	179
	:57.3		6300	1.52	1.33	.19	330
	36:09.3		6435	1.84	1.26	.58	174
	:21.3		7100	1.72	1.20	.52	175
	:33.3		8200	1.54	1.16	.38	206
	:47.3		4000	1.38	1.10	.28	187
	:59.3		4760	1.63	1.02	.61	141
	37:11.3		5080	1.54	.95	.59	148
	:23.3		5300	1.51	.90	.61	147
	:35.3		5577	.98	.79	.19	214
	:49.4		6080	1.19	.69	.50	159
	38:01.4		6300	.81	.60	.21	373
	:13.3		6435	1.01	.53	.48	145
	:25.3		7100	.91	.45	.46	153
	:37.3		8200	.69	.35	.34	183
	:51.5		4000	.53	.28	.25	166
	39:03.5		4760	.84	.28	.56	129
	:15.5		5080	.83	.22	.61	153
	:27.5		5300	.83	.19	.64	152
	:39.5		5577	.30	.17	.13	149
	:53.5		6080	.62	.15	.47	149
	40:05.5		6300	.22	.13	.09	166
	:17.5		6435	.63	.12	.51	154
	:29.5		7100	.60	.12	.48	159
	:41.5		8200	.44	.11	.33	180
	:55.5		4000	.36	.11	.25	163
	41:07.6		4760	.70	.11	.59	136
	:19.6		5080	.72	.11	.61	154
	:31.6		5300	.74	.11	.63	151
	:43.6		5577	.26	.11	.15	169
	:57.6		6080	.56	.10	.46	148
	42:09.6		6300	.21	.10	.11	198
	:21.6		6435	.61	.10	.51	153
	:33.6		7100	.58	.10	.48	161
	:45.6		8200	.44	.10	.34	182

APPENDIX 2

Air Mass versus Altitude and Apparent and Geometric Sunrise and Sunset seen from Skylab

Utilizing techniques given in Schuerman, et al. (1975)* the apparent altitude of the rising/setting sun was calculated as a function of time (Table 1), taking account of the effects of beta angle and refraction. To illustrate use of the table, the apparent sunrise at beta angle 30° is 27 seconds before geometric sunrise, and the sun is at an apparent altitude of 10 km 26 seconds after apparent sunrise.

At each altitude the sun's rays are seen through a different air mass. The geometry used to determine the appropriate air mass is shown below.

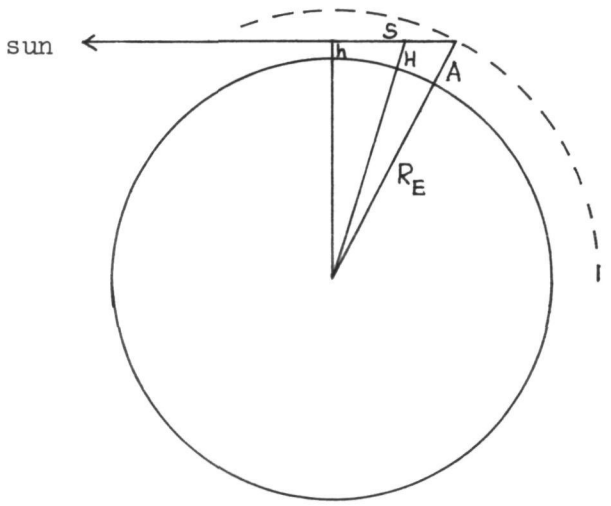

A spacecraft altitude
h apparent altitude of sun
s 1/2 the path traversed by the sun's rays
H altitude at any point along s
h_T extent of atmosphere ≈120 km

---

* D.W. Schuerman, F. Giovane, and J.M. Greenberg, Stellar Refraction: A Tool to Monitor the Height of the Tropopause from Space, J. Appl. Meteorol. 14, 1182-1186, 1975.

The total air mass m along path s is

$$\frac{2\int_{h}^{h_T} \rho(H)\, ds(H)}{\int_{0}^{h_T} \rho(H)\, dH},$$

where $\rho(H)$ is taken from the U.S. Standard Atmosphere Supplements, 1966. Since

$$ds(H) = \frac{(H + R)\, dH}{\sqrt{(H + R)^2 - (h + R)^2}},$$

$$m = \frac{2\int_{h}^{h_T} \frac{\rho(H)(H + R)\, dH}{\sqrt{(H + R)^2 - (h + R)^2}}}{\int_{0}^{h_T} \rho(H)\, dH}.$$

m was calculated at 2 km intervals of altitude H from 0 to 70 km; the results are given in Table 2.

Table 1

Apparent Sun Rise/Set Time versus Altitude

beta angle	T(0)	ΔT10	20	30	40	50	60	70	80	90	100
0	:23	:22	:30	:34	:38	:42	:46	:50	:54	:58	1:02
5	:23	:22	:30	:34	:38	:42	:46	:50	:54	:58	1:03
10	:23	:23	:30	:35	:39	:43	:47	:51	:55	:59	1:03
15	:24	:23	:31	:36	:40	:44	:48	:52	:56	1:01	1:05
20	:25	:24	:32	:37	:41	:45	:49	:54	:58	1:03	1:07
25	:26	:25	:33	:38	:43	:47	:52	:56	1:01	1:05	1:10
30	:27	:26	:35	:40	:45	:50	:54	:59	1:04	1:09	1:14
35	:29	:28	:38	:43	:48	:53	:58	1:03	1:08	1:14	1:19
40	:32	:31	:41	:47	:53	:58	1:03	1:09	1:14	1:20	1:26
45	:35	:34	:45	:52	:58	1:04	1:10	1:16	1:22	1:29	1:35
50	:41	:39	:52	:60	1:07	1:13	1:20	1:27	1:34	1:41	1:48
55	:48	:46	1:02	1:11	1:19	1:27	1:35	1:43	1:51	1:59	2:08
60	1:03	1:00	1:20	1:31	1:42	1:52	2:02	2:12	2:22	2:32	2:42
61	1:07	1:04	1:25	1:38	1:49	1:59	2:10	2:20	2:31	2:41	2:52
62	1:12	1:10	1:32	1:45	1:57	2:08	2:19	2:30	2:42	2:53	3:04
63	1:19	1:16	1:40	1:55	2:07	2:19	2:31	2:43	2:55	3:07	3:19
64	1:28	1:25	1:51	2:07	2:20	2:33	2:46	2:59	3:12	3:25	3:38
65	1:40	1:37	2:06	2:23	2:38	2:52	3:07	3:21	3:35	3:48	4:02
66	1:59	1:55	2:28	2:48	3:05	3:21	3:36	3:52	4:07	4:22	4:38
67	2:35	2:30	3:10	3:32	3:52	4:10	4:28	4:45	5:02	5:19	5:36
68		5:04	5:55	6:23	6:47	7:08	7:20	7:50	8:10	8:29	8:48
69		2:37	4:04	4:44	5:16	5:44	6:11	6:36	7:00	7:23	7:46
70				1:36	2:49	3:39	4:20	4:56	5:28	5:59	6:27

T(0) is the difference between the time of apparent sunrise (sunset) and the time of geometric sunrise (sunset). Geometric rise and set have SA (solar depression angle) = 110.5957 deg. for OWS alt. of 435 km., while apparent rise and set have SA = 112.0854 deg.

T10, 20, etc., are the time intervals between apparent rise (set) and the time the sun appears to be at 10, 20, etc. km. Times are in min:sec.

Table 2

Air Mass versus Altitude

Altitude(km)	Total air mass	Altitude(km)	Total air mass
0	78.0	36	.41
2	63.2	38	.31
4	50.16	40	.23
6	39.32	42	.17
8	30.38	44	.13
10	23.04	46	.10
12	16.96	48	.08
14	12.38	50	.06
16	9.04	52	.05
18	6.60	54	.04
20	4.82	56	.03
22	3.52	58	.02
24	2.58	60	.02
26	1.88	62	.01
28	1.38	64	.01
30	1.02	66	.01
32	.76	68	.00
34	.56	70	.00

APPENDIX 3

Irradiance at the Spacecraft due to the Sunlit Earth as a Function of Time

The solar depression angle T is defined in the following figure:

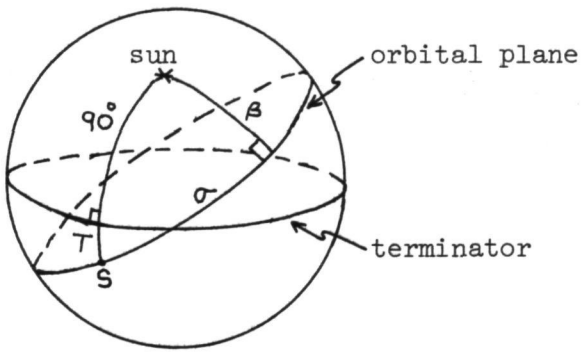

s position of spacecraft
β beta angle
T solar depression angle

From the above, we obtain

$$\cos (90^\circ + T) = \cos \sigma \cos \beta \qquad (1)$$

or $$\sin T = -\cos \sigma \cos \beta. \qquad (2)$$

T is 20.55° at sunrise/sunset and 0° at terminator rise. Since $\frac{d\sigma}{dt}$ is known to be 3.87°/min (orbital angular velocity), $\frac{dT}{dt}$ can be calculated from (2).

The area of the sunlit earth seen by the spacecraft is illustrated below.

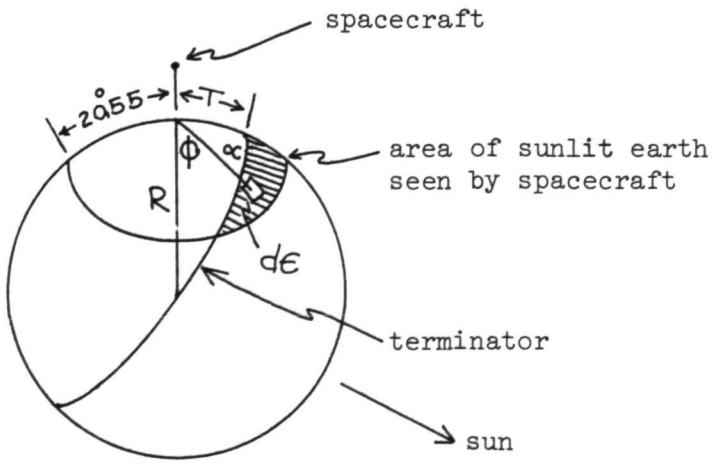

To derive this area as a function of solar depression angle T, we note that

$$d\epsilon = R^2 \sin\alpha \, d\alpha d\phi. \tag{3}$$

The total area A is then

$$A(T) = \int d\epsilon = R^2 \int_{T_1}^{T_2} \sin\alpha \, d\alpha \int_{\phi_1}^{\phi_2} d\phi. \tag{4}$$

To determine the value of A at any value of T, the appropriate limits of integration are:

$$T_1 = 20.55^\circ$$

$$T_2 = T$$

$$\phi_1 = \sin^{-1} \frac{\tan T}{\tan \alpha} \qquad \text{(equation of terminator)}$$

$$\phi_2 = \pi.$$

The area A' projected on a plane perpendicular to the spacecraft-earth line is

$$A'(T) = 2R^2 \int_{20.6}^{T} \cos\alpha \sin\alpha \, d\alpha \left[\frac{\pi}{2} - \sin^{-1}\left(\frac{\tan T}{\tan \alpha}\right)\right]. \tag{5}$$

The brightness of the area A is a function of the reflection coefficient $F(\lambda)$ and the irradiance of the sun on the area:

$$B_A \propto I_\odot \, F(\lambda) \, e^{-\tau(\lambda) \, m \, (T)}, \tag{6}$$

where $\tau(\lambda)$ is the absorption of unit air mass, m(T) is the number of air masses traversed, and $I_\odot$ is the solar irradiance. The irradiance at the spacecraft is then

$$I_s(T) \propto B_A A' e^{-\tau(\lambda)\, m\,(T)} \tag{7}$$

or

$$I_s(T) \propto A'(T)\, F(\lambda)\, I_\odot\, e^{-2\tau(\lambda)\, m\,(T)}. \tag{8}$$

$F(\lambda)$ is assumed to be a constant and $I_\odot$ is known. Thus

$$I_s(T) \propto A'(T)\, e^{-2\tau(\lambda)\, m\,(T)}. \tag{9}$$

The function $m(T)$ can be determined from

$$\cos(T + 2\theta) = \frac{R}{R + h} \cos\theta\ , \tag{10}$$

where θ is the solar elevation angle, R is the radius of the earth, and h is the spacecraft altitude.

(T) is determined from (10) and $m(\theta)$ is obtained from Allen (1973). Therefore, $m(T)$ is the product of the functions $\theta(T)$ and $m(\theta)$, and $I_s(T)$ can be determined. Since $T(t)$ can be determined from (2), $I_s(t)$ can be

NASA-Langley, 1976

NATIONAL AERONAUTICS AND SPACE ADMINISTRATION
WASHINGTON, D.C. 20546

OFFICIAL BUSINESS
PENALTY FOR PRIVATE USE $300

SPECIAL FOURTH-CLASS RATE
BOOK

POSTAGE AND FEES PAID
NATIONAL AERONAUTICS AND
SPACE ADMINISTRATION
451

U.S.MAIL

POSTMASTER: If Undeliverable (Section 158 Postal Manual) Do Not Return

"The aeronautical and space activities of the United States shall be conducted so as to contribute . . . to the expansion of human knowledge of phenomena in the atmosphere and space. The Administration shall provide for the widest practicable and appropriate dissemination of information concerning its activities and the results thereof."

—NATIONAL AERONAUTICS AND SPACE ACT OF 1958

NASA SCIENTIFIC AND TECHNICAL PUBLICATIONS

TECHNICAL REPORTS: Scientific and technical information considered important, complete, and a lasting contribution to existing knowledge.

TECHNICAL NOTES: Information less broad in scope but nevertheless of importance as a contribution to existing knowledge.

TECHNICAL MEMORANDUMS: Information receiving limited distribution because of preliminary data, security classification, or other reasons. Also includes conference proceedings with either limited or unlimited distribution.

CONTRACTOR REPORTS: Scientific and technical information generated under a NASA contract or grant and considered an important contribution to existing knowledge.

TECHNICAL TRANSLATIONS: Information published in a foreign language considered to merit NASA distribution in English.

SPECIAL PUBLICATIONS: Information derived from or of value to NASA activities. Publications include final reports of major projects, monographs, data compilations, handbooks, sourcebooks, and special bibliographies.

TECHNOLOGY UTILIZATION PUBLICATIONS: Information on technology used by NASA that may be of particular interest in commercial and other non-aerospace applications. Publications include Tech Briefs, Technology Utilization Reports and Technology Surveys.

Details on the availability of these publications may be obtained from:

SCIENTIFIC AND TECHNICAL INFORMATION OFFICE

NATIONAL AERONAUTICS AND SPACE ADMINISTRATION

Washington, D.C. 20546